HETEROEPITAXY OF GASB ON GAAS (111)A FOR ELECTRON TRANSPORT STUDIES

by

Madison Drake

A thesis

submitted in partial fulfillment

of the requirements for the degree of

Master of Science in Material Science and Engineering

Boise State University

December 2022

BOISE STATE UNIVERSITY GRADUATE COLLEGE

DEFENSE COMMITTEE AND FINAL READING APPROVALS

of the thesis submitted by

Madison Drake

Thesis Title: Heteroepitaxy of GaSb on GaAs (111)A for Electron Transport Studies

Date of Final Oral Examination: 16 September 2022

The following individuals read and discussed the thesis submitted by student Madison Drake, and they evaluated the student's presentation and response to questions during the final oral examination. They found that the student passed the final oral examination.

Paul J. Simmonds, Ph.D.	Chair, Supervisory Committee
Dave Estrada, Ph.D.	Member, Supervisory Committee
Eric Jankowski, Ph.D.	Member, Supervisory Committee

The final reading approval of the thesis was granted by Paul J. Simmonds, Ph.D., Chair of the Supervisory Committee. The thesis was approved by the Graduate College.

DEDICATION

I would like to dedicate this thesis to my family and friends.

Without the endless enthusiasm of my mother, Kristi Drake, I would never have believed in myself enough to pursue my dreams.

Without the logic and reasoning of my father, Craig Drake, I would not have been in a position to make this dream a reality.

Without the constant support of my fiancé, Andrew Nordstrom, I would not have survived the stress of graduate school.

Without the encouragement of my sister, Emmy Drake, and my friends both near and far, the trials and tribulations I have faced both in graduate school and the choices leading me here would have been daunting and hard to overcome.

This network of people has supported me and made me the scientist I am today, for which I am forever grateful.

ACKNOWLEDGMENTS

I would like to start by acknowledging the work of several of my high school science teachers. This specific group of people laid the ground work for me to become the scientist I am today. Mr. Steve Greene encouraged me to pursue physics when I was a freshman in high school and helped me set up a path to be prepared to go into this field in college. This encouragement set me on the path I am today. Mr. John Miller and Dr. Russ Lord also played a pivotal role in my high school science education. They taught me that science did not have to exclude creativity, and that when a more creative approach is taken to scientific thinking novel ideas can be formed.

I would also like to acknowledge several of my college undergraduate professors. Dr. David Macaluso believed in me and allowed me to join his lab. I learned more than I could have imagined being in this lab and learned how to be a more independent researcher. Dr. Eijiro Uchimoto and Dr. Paul Janzen also played pivotal roles in my scientific education, and I would not be the same researcher I am today without the valuable lessons they imparted to me.

Most critically, I would like to acknowledge the work of the many collaborators I have had the opportunity to work with for this project. The members of the surface science lab, specifically Victor Nguyen, who have helped make this work possible. I would also like to thank Kunal Mukherjee and Pooja Reddy for their assistance in getting ECCI and the additional ideas they have had for this project. Additional I would like to thank Kevin Grossklaus for his help getting TEM. Finally, I would like to thank Kevin

Vallejo, Cody Dennet, Krzysztof Gofryk, and Narayan Poudel for their help getting magnetoresistance measurements.

I would also like to acknowledge my lab coworker, Trent Garrett. Trent is a very hard working individual and his joining the lab made it a much more pleasant experience. And most importantly, I would like to acknowledge my advisor and mentor Paul Simmonds. Paul has taught me so many new things and has always kept my background in perspective when he is teaching me something to make it more applicable.

This group of mentors and coworkers has made me the scientist I am today. I am so grateful to have known them and had the opportunity to work with and learn from them.

ABSTRACT

III-V semiconductors grown by molecular beam epitaxy (MBE) on (111) surfaces have some interesting electronic properties. For certain materials with a (111)-orientation, the Γ- and L-valleys are reasonably close in energy. This means that it may be possible to take advantage of electron conduction in the L- and Γ-valleys at the same time, allowing us to overcome the so-called "density-of-states bottleneck," and enable transistors with large drive currents.[1] We have investigated this phenomenon in GaSb- and InAs-based 2D electron gases for which the electron effective masses are low.

However, growth of materials with a (111) orientation is typically more challenging than on traditional (001) surfaces. The MBE conditions needed to grow high quality material are often poorly understood.[2] We began by exploring InAs/GaSb quantum well (QW) structures,[3] grown directly on GaSb(111)A substrates. This work shows that low growth rates under very high group V overpressures produce good GaSb homoepitaxy and InAs heteroepitaxy, as characterized by XRD and AFM. However, although we have been able to identify MBE conditions that lead to the growth of smooth, high-quality material, GaSb(111)A substrates are extremely expensive, as well as being intrinsically *n*-type, which complicates the carrier transport measurements in which we are interested. If we could instead grow our GaSb-based QW structures on cheaper, non-conductive GaAs(111)A substrates, we could overcome these issues. The challenge is the large lattice mismatch between GaSb and GaAs, which typically results in strain-driven crystallographic disorder at the heterointerface and poor material quality.

One technique that has shown promise in circumventing these problems on (001) surfaces is the use of interfacial misfit arrays (IMFs). Under specific molecular beam epitaxy (MBE) conditions it is possible to produce an array of 90° dislocations that lie in the GaSb/GaAs(001) heterointerface. These dislocations efficiently relieve the strain between the two materials without generating the high density of threading dislocations that one would ordinarily expect. As a result, it is possible to grow high quality materials and active device structures above these IMF-based heterointerfaces.

This thesis describes our work to extend a modified version of this IMF technique to (111) surfaces in order to grow our InAs/GaSb QW structures on GaAs(111)A substrates. So far, this work has produced GaSb grown on GaAs (111)A with a full-width-half-maximum (FWHM) XRD peak value of 124''. For GaSb/GaAs(001) grown via an IMF approach, other groups have reported FWHM values of 240''.[4] This work shows how various MBE parameters such as growth temperature, Sb overpressure, GaSb growth initiation and GaSb growth rate affect IMF formation. This thesis also reports initial electron transport measurements from InAs/GaSb QWs grown on GaAs(001) and (111) substrates via this IMF technique.

TABLE OF CONTENTS

DEDICATION iv

ACKNOWLEDGMENTS v

ABSTRACT vii

LIST OF FIGURES xi

LIST OF ABBREVIATIONS xv

CHAPTER ONE: INTRODUCTION AND BACKGROUND 1

1.1 Project Motivation and History 1

1.2 III-V Semiconductors 4

1.2.1 General Semiconductor Background 4

1.2.2 6.1 Å Family of Materials 6

1.3 2-Dimensional Electron Gases 7

1.4 Interfacial Misfit Arrays 14

1.5 Previous Work 16

CHAPTER TWO: EXPERIMENTAL METHODS 17

2.1 Molecular Beam Epitaxy 17

2.2 Reflection High Energy Electron Diffraction 20

2.3 X-ray Diffraction 23

2.4 Atomic Force Microscopy 24

2.5 Transmission Electron Microscopy 25

2.6 Scanning Transmission Electron Microscopy and Electron Energy Loss Spectroscopy 26

2.7 Electron Channel Contrast Imaging 27

2.8 Magnetoresistance Measurements 28

CHAPTER THREE: RESULTS AND DISCUSSION 30

3.1 General 30

3.2 InAs/GaSb QW samples grown on (001) substrate orientation 31

3.2.1 Growth on GaSb(001) substrates 31

3.2.2 Growth on GaAs(001) substrates 34

3.3 InAs/GaSb QW samples grown on (111)A substrate orientation 38

3.3.1 Growth on GaSb(111)A substrates 38

3.3.2 Growth on GaAs(111)A substrates 41

FUTURE WORK 62

REFERENCES 64

LIST OF FIGURES

Figure 1.1 Band structure and alignment for GaSb5 3

Figure 1.2 Direct and indirect band gap structures6 5

Figure 1.3 Band alignment for the three types of heterostructures7 6

Figure 1.4 Band gap energy vs lattice constant for compound semiconductor III-V materials8 7

Figure1.5 MOSFET schematic9 8

Figure 1.6 A) Flat band diagram for MOSFET without gate voltage supplied10 B) Band structure for MOSFET in inversion mode11 9

Figure 1.7 Band structure for a quantum well12 10

Figure 1.8 Classic Hall Effect13 11

Figure 1.9 a) Electron cyclotron motion b) fermi energy across structure c) net effect on electron motion14 12

Figure 1.10 Quantum hall effect measurement with hall plateaus shown in red and Shubnikov-de Haas oscillations shown in black12 13

Figure 1.11 IMF bonding schematic15 16

Figure 2.1 Schematic of an MBE chamber16 18

Figure 2.2 Atomic process occurring as a layer is formed A) atom arrives at the surface and adsorbs, B) atom diffuses across surface C) atom arrives at the step edge and forms step edge growth, D) atomic terraces formed through step edge growth E) island nucleation F) desorption of atom 16 20

Figure 2.3 A schematic with the RHEED set up and sample stage17. A) a wafer with the thermal oxide present, B) a clean 2x pattern showing the oxide has been removed, C) and additional 5x pattern that can be seen as the sample is rotated 21

Figure 2.4 a) RHEED pattern with RIOs collection area highlighted, b) signal collected out of pattern area46 c) monolayer growth stage, surface schematic, and corresponding RIOs graph46 22

Figure2.5 Reciprocal space map for GaSb peak showing the difference between rocking curve and 2 theta scans, and a 2 theta scan with a rocking curve inset4 24

Figure 2.6 Schematic of how an AFM probe generates an image18 with a sample image taken from a GaSb surface 25

Figure2.7 Schematic of a TEM set up19..... 26

Figure 2.8 A schematic for a STEM (essentially the same as the TEM but containing the EELS equipment) B) schematic for EELS measurement20 27

Figure 2.9 Schematic and image types for ECCI. A&B) types of geometry possible, C&D) types of images created21 28

Figure 2.10 Quantum hall effect measurement with hall plateaus shown in red and Shubnikov-de Haas oscillations shown in black12..... 29

Figure 3.1 Sample structure and band alignment for this structure..... 30

Figure 3.2 a) 50x50 □m2 scan with Rq =5.0Å. b) 2x2□m2 scan with Rq = 1.1Å.... 32

Figure 3.3 XRD 2theta omega scan with FWHM of 199.5”..... 33

Figure 3.4 Longitudinal magnetoresistance measurements performed at INL showing Shubnikov-de Haas oscillations resolvable up to 20K..... 34

Figure 3.5 a) reference image from the literature[3] b) 50 × 50 μm^2 scan , Rq = 1.4 nm c) 2 × 2 μm^2 scan, Rq = 1.0 nm with inset of peak of defect 36

Figure 3.6 2 θ/ω XRD with GaSb(001) peak FWHM of 228.3”. Inset shows rocking curve scan or the GaSb peak with FWHM of 318.9”. 37

Figure 3.7 50x50μm^2 scans for A) Ga growth rate=0.3ML/s, Sb flux=2.8E-6, rq=2.59 nm , B) Ga growth rate=0.13 ML/s, Sb flux=4E-6, rq=3.83nm , C) Ga growth rate=0.13 ML/s, Sb flux=3E-6, rq=3.14nm..... 39

Figure 3.8 2x2μm^2 scans for A) Ga growth rate=0.3ML/s, Sb flux=2.8E-6, rq=0.452nm , B) Ga growth rate=0.13 ML/s, Sb flux=4E-6, rq=0.144nm , C) Ga growth rate=0.13 ML/s, Sb flux=3E-6, rq=0.123nm..... 40

Figure 3.9 XRD 2θ/ω scans for A) GaSb growth rate=0.3ML/s, Sb flux=2.8E-6 Torr, FWHM=125.6", B) GaSb growth rate=0.13 ML/s, Sb flux=4E-6 Torr, FWHM=168.5", C) GaSb growth rate=0.13 ML/s, Sb flux=3E-6 Torr, FWHM=75.9". 41

Figure 3.10 80x80 μm^2 AFM scans A) 3E-6 SbTorr flux, rq= 11.8nm , B) 4E-6 Sb Torr flux, rq=10.8nm 42

Figure 3.11 2x2 μm^2 AFM scans A) 2E-6 Sb Torr flux, rq= 3.8nm , B) 3E-6 Sb Torr flux, rq= 4.5nm C) 4E-6 Sb Torr flux, rq=1.69nm....43

Figure 3.12 XRD 2θ/ω scans with rocking curve inset A) 2E-6 Sb Torr flux, FWHM=353.2" , B) 3E-6 Sb Torr flux, FWHM= 498.6" C) 4E-6 Sb Torr flux, FWHM=124.7" 44

Figure 3.13 ECCI scans A) 2E-6 Sb Torr flux, TDD=2.3E8 , B) 3E-6 Sb Torr flux, TDD= 2.7E8 C) 4E-6 Sb Torr flux, TDD=2.8E8 45

Figure 3.14 ECCI out of channeling scans A) 2E-6 Sb Torr flux, B) 3E-6 Sb Torr flux C) 4E-6 Sb Torr flux....46

Figure 3.15 TEM of large defect free region performed on 4E-6 Torr sample 47

Figure 3.16 a) Zoomed in TEM to show the IMF b) closer view of the IMF c) atomic bond bend to form the IMF 48

Figure 3.17 EELS of IMF interface region to confirm elemental signatures....48

Figure 3.18 TEM of defects in the 4E-6 Torr sample with A) coming from the IMF region and B) coming from the QW region 49

Figure 3.19 Magnetoreistance data on 4E-6 Torr sample showing Shubnikov-de Haas oscillations 50

Figure 3.20 Test structures for GaAs (111)A optimization....51

Figure 3.21 50 × 50μm^2 AFM scans for A) control structure, rq=5.19nm, B)10nm SL layers, rq=5.27nm, C) 5nm SL layers, rq=20.9nm, D) 10 degrees cooler, rq=8.48nm, E) 20 degrees cooler, rq=7.81nm 52

Figure 3.22 2x2μm^2 AFM scans for A) control structure, rq=2.45nm, B)10nm SL layers, rq=0.829 nm, C) 5nm SL layers, rq=1.67 nm, D) 10 degrees cooler, rq=0.366 nm, E) 20 degrees cooler, rq=0.325 nm 53

Figure 3.23 XRD 2θ/ω scans for A) control structure, FWHM=200.9", B)10nm SL layers, FWHM=168.5", C) 5nm SL layers, FWHM=164.5", D) 10 degrees cooler, FWHM=180.0", E) 20 degrees cooler, FWHM=181.8" 54

Figure 3.24 XRD Rocking curve scans for A) control structure, FWHM=353.2", B)10nm SL layers, FWHM=350.0", C) 5nm SL layers, FWHM=554.0", D) 10 degrees cooler, FWHM=244.8", E) 20 degrees cooler, FWHM=202.0" 55

Figure 3.25 A) the 50x50μm^2 AFM scan, rq=8.47nm, B) the 2x2μm scan, rq=0.615nm for the combined SL and temperature change structure..... 56

Figure 3.26` XRD scans for combined SL and temperature change test structure with 2θ/ω FWHM=130.3 "and Rocking curve inset FWHM=381.6"..... 56

Figure 3.27 50x50μm^{2}AFM scans for A) SL and temp change, rq=10.8nm, B) Temp change only rq=11.2nm, C) previous best sample with 4E-6 flux, rq=10.8nm. 58

Figure 3.28 2x2μm^2 AFM scans for A) SL and temp change, rq=0.445 nm, B) Temp change only rq=0.327nm, C) previous best sample with 4E-6 flux, rq=1.69nm. 59

Figure 3.29 XRD scans for A) SL and Temp change, FWHM =478.8", B) Temp change only, FWHM 396.0", C) Previous best sample FWHM=124.7".. 60

Figure 3.30 Magnetoresistance measurements for A) the SL and temperature change defect filtered sample and B) the temperature change only defect filtered sample..... 61

LIST OF ABBREVIATIONS

2DEG	2-Dimensional Electron Gas
QHE	Quantum Hall Effect
QW	Quantum Well
IMF	Interfacial Misfit Array
LED	Light Emitting Diode
VBM	Valence Band Maximum
CBM	Conduction Band Minimum
HEMT	High Electron Mobility Transistor
MOSFET	Metal-Oxide-Semiconductor Field Effect Transistor
MBE	Molecular Beam Epitaxy
Si	Silicon
Ga	Gallium
Sb	Antimony
As	Arsenic
In	Indium
Al	Aluminum
Mo	Molybdenum
RHEED	Reflection High Energy Electron Diffraction
RIOs	RHEED Intensity Oscillations
XRD	X-ray Diffraction
FWHM	Full Width Half Maximum
AFM	Atomic Force Microscopy
TEM	Transmission Electron Microscopy
FIB	Focused Ion Beam
STEM	Scanning Transmission Electron Microscopy
EELS	Electron Energy Loss Spectroscopy
ECCI	Electron Channel Contrast Imaging
SEM	Scanning Electron Microscopy
Rq	RMS roughness
INL	Idaho National Laboratory
BSU	Boise State University
TDD	Threading Dislocation Density
SL	Superlattice
PL	Photoluminescence

CHAPTER ONE: INTRODUCTION AND BACKGROUND

1.1 Project Motivation and History

Since the advent of 2-dimensional electron gases (2DEGs), new physics and applications have astounded the world. 2DEGs allow for the confinement of carriers in one spatial dimension such that their energy becomes quantized in that direction.[10] The invention of the 2DEG led to the discovery of the quantum Hall effect (QHE) in 1980.[22] The QHE is a powerful tool for probing the fundamental physics of electrons and discovering new phenomena. In particular this effect allows for the exploration of spin polarization and splitting.

The traditional materials system of interest for 2DEGs involves the confinement of electrons within a GaAs quantum well (QW), with confinement produced by AlGaAs barriers.[23] There are several reasons why these systems have been a focus. First, the matching lattice constants of GaAs and AlGaAs allow for fabrication with minimal strain in the device.[23] This means one can grow arbitrarily wide quantum wells enabling one to control the energy of the quantum confined ground state. Second, the ternary nature of AlGaAs barriers allows one to tune the height of the barriers. Third, efficient modulation doping enables one to tailor the electron density within the 2DEG while minimizing scattering from ionized impurity centers.[23] With such a robust and well-studied system in place, one might conclude that no more work needs to be done here.

However, researchers have shown that 2DEGs formed in other material systems may offer useful and interesting behaviors that are not exhibited in the traditional

GaAs/AlGaAs system. An example of this is the use of InAs as the QW layer. InAs has a lower electron effective mass (= $0.032m_0$)[24] than GaAs (= $0.067m_0$),[25] which could help increase electron mobility, as well as a larger Landé g-factor (= 11.5)[24] for high spin-orbit coupling.[26] The lattice constant of InAs (= 6.06 Å)[27] makes it well-suited for incorporation with GaSb (= 6.10 Å)[27] barriers as their lattice constants are nearly matched with only a 0.66% mismatch.

The narrow band gaps that one can access with the InAs/GaSb material system means that it is well-suited to infrared optoelectronics applications. However, we can also take advantage of the type-III "broken gap" band alignment between these materials and their large spin-orbit coupling to achieve band inversion and create topologically protected states in double or triple QW structures.[28] These protected states exhibit spin-momentum locking, such that electrons in these states can effectively travel without scattering, with implications for spintronics, low-powered electronics, and quantum computing.[29,30]

Another interesting feature of the InAs/GaSb QW structures comes from the crystallographic orientation with which we grow them. As we move away from growth on the traditional (001) orientation we are able to access some new and interesting properties. III-V semiconductors typically exhibit lower electron effective masses than Si, which is of interest for high mobility transistor devices. The issue is, however, that (001)-oriented III-V materials usually have lower density of states in the conduction band than Si, an issue known as the density of states bottleneck.[2,31] One way to overcome this is to work instead with (111)-oriented III-V materials.[2] The (111) orientation allows for access to the L-valley for electron transport, which has a higher density of states.[2] For this to

work we need to work with materials such as GaSb(111)A for which the energy barrier between the Γ and the L valleys is small (Figure 1.1), and electron transport can hence occur in both simultaneously.[2] What we can see, therefore, is that 2DEGs based on the InAs/GaSb QW system, particularly with a (111) surface orientation, have some distinct advantages over the traditional GaAs/AlGaAs(001) QW system.

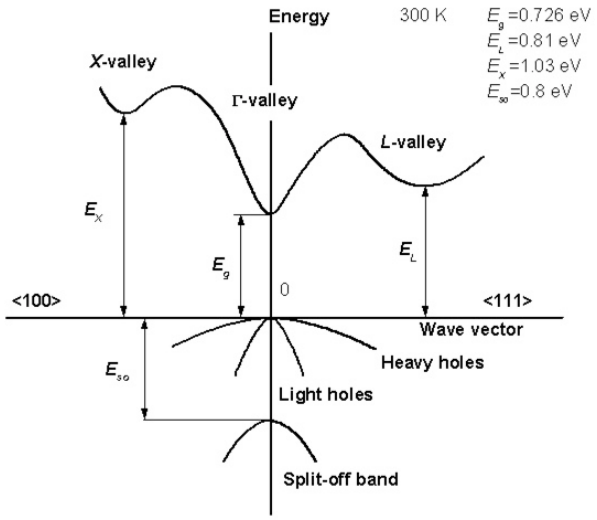

Figure 1.1 Band structure and alignment for GaSb5

There are, however, some challenges that we must overcome before we can explore the viability of InAs/GaSb-based 2DEGs for these applications. The first concerns the GaSb substrate wafers upon which we would like to grow these structures. GaSb is quite expensive (~5x more expensive that GaAs(001)), and even more expensive for substrates cut with a non-traditional (111)A orientation. In addition, unlike GaAs substrates, GaSb substrates are conductive due to a high intrinsic p-doping, which complicates carrier transport measurements since we do not know whether the carriers are moving in the 2DEG, the substrate, or both. GaAs would therefore be a preferable substate material but GaAs is highly lattice mismatched to both GaSb (8.0% mismatch) and InAs (7.3% mismatch), making strain management a significant problem. Such high

strains are typically relaxed in a few nanometers of the GaSb/GaAs interface through the formation of threading dislocations that destroy the properties of any overlying GaSb-based devices. For the (001) surface, researchers have previously explored the use of an interfacial misfit array (IMF) to effectively relieve these large strains at the GaSb/GaAs interface without the formation of threading dislocations.[3] However, this approach has yet to be extended to growth of highly mismatched materials on (111)-oriented substrates.

To explore the properties of 2DEGs confined within non-traditional InAs/GaSb QWs, particularly for a (111)A surface orientation, I decided to focus this thesis research on modulation-doped InAs/GaSb QW structures grown on GaAs(001) and GaAs(111)A surfaces.

1.2 III-V Semiconductors

1.2.1 General Semiconductor Background

Semiconductors are among the most important materials in the world today due to their wide variety of applications. They are the basis for memory devices as well as many optoelectronic applications, from light emitting diodes (LEDs) for displays, photovoltaics for renewable energy applications, and laser systems for telecommunications.[32] Most memory-based semiconductors use silicon (Si) for their starting point. However, the indirect band gap of Si means that it is not suitable for light emitting optoelectronic applications.

When assessing band structure, direct band gap materials have their valence band maximum (VBM) and conduction band minimum (CBM) aligned in k-space (Figure 1.2).[33] This allows electrons at the CBM to recombine with holes at the VBM without

any change in momentum, which means they do not require any phonon interactions. For indirect band gap materials, the VBM and CBM do not lie at the same location in k space (Figure 1.2). In order for an electron at the CBM to recombine with a hole at the VBM, it must not only change its energy but also its momentum value, or k value, which requires a phonon interaction.[33] Due to this additional requirement to emit light, indirect band gap materials do not make efficient light emitters.

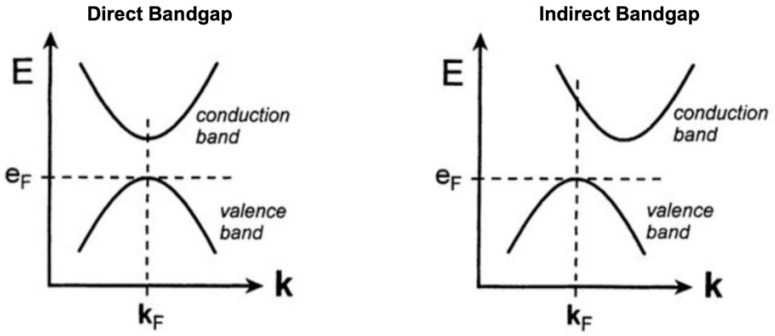

Figure 1.2 Direct and indirect band gap structures6

Si is an elemental semiconductor due to its four valence electrons. Compound semiconductors can be fabricated by combining multiple elements, many of which have compositions that offer a direct band gap. There are several families of these compound semiconductors including the III-Vs and II-VIs. By combining different elements in certain ratios, it is possible to engineer these materials to have the bandgap needed to emit and absorb light at certain wavelengths for specific applications.[32]

We can form heterostructures from these III-V materials. A heterostructure is simply the layering of two dissimilar semiconductor materials with different band profiles to create different devices.[34] There are essentially three types of heterostructure, (Figure 1.3). For type-I heterostructures the energy gap between the conduction band and the valence band are both smaller in one material than the other.[7] In type-II

heterostructures, one material has a band gap that is offset from the other material such that the bottom of the conduction and valence band in one material is higher than that of the other, however a continuous band gap is maintained across the heterojunction. Type-III heterostructures are similar to type-II except that we see an overlap between the VBM of one material with the CBM of the other across the heterojunction.[7] Taken in combination these three heterostructures are the basis for a wide range of electronic and optoelectronic devices including high electron mobility transistors (HEMTs), lasers, photodetectors, and solar cells. HEMTs, whose channel is based on the confinement of a 2DEG within a QW will be predominantly of interest for this work.

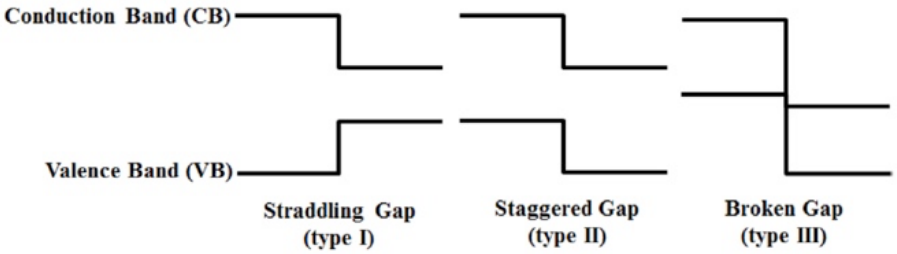

Figure 1.3 Band alignment for the three types of heterostructures7

1.2.2 6.1 Å Family of Materials

InAs, GaSb, and AlSb form what is called the 6.1Å family of materials. A graph showing the bandgap vs lattice constant of several commonly encountered semiconductor materials is shown in Figure 1.4. The 6.1Å family (circled in blue) gets its name from the fact that these materials all have lattice constants near 6.1Å [27] The similar lattice constants of these materials means we can combine them into heterostructures with minimal strain. The band gap energies of these materials vary from 0.36 eV for InAs to 1.61 eV for AlSb, which are well-suited to infrared optoelectronics across a fairly wide wavelength range.[27] Of particular interest is the fact that these materials permit different band lineups from the

traditional GaAs/AlGaAs materials system, giving us access to various heterostructure types.[27] The InAs/GaSb system which is the basis for this thesis research is particularly interesting because it presents a type-III or broken gap heterostructure. This means that at the interface of these two materials the CBM of the InAs lies below the VBM of the GaSb. In effect, when confined states are present, this makes very deep quantum wells possible which is particularly valuable because it creates high tunneling barriers and very strong quantization.[27] Superlattices based on InAs/GaSb type-III heterostructures are widely used for infrared photodetectors.

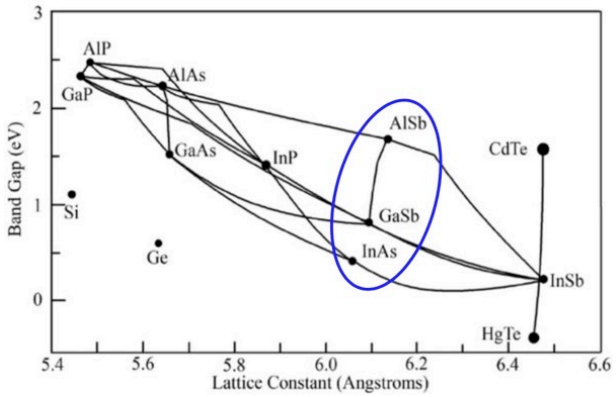

Figure 1.4 Band gap energy vs lattice constant for compound semiconductor III-V materials8

1.3 2-Dimensional Electron Gases

A 2DEG is an electron gas that is quantum confined so it can only move in two dimensions. In a bulk material, an electron can have any range of energies. However, confining electrons to a two-dimensional QW causes their energies in the out-of-plane direction to be quantized into discrete levels. By doing this, we can manipulate the electronic properties of the material to be significantly different from those of the bulk material.

One of the simplest and most well-known 2DEGs is the metal-oxide-semiconductor field effect transistor, or MOSFET.[10] A MOSFET is made using a doped Si substrate and layering an insulating oxide followed by a metal to form the gate. There are also source and drain regions formed in the Si outside of, but near to the gate with the opposite doping. For instance, the Si under the gate could be p-doped (group III materials that add an extra hole) while the Si under the source and the drain could be n-doped (group V materials that add an extra electron), or vice versa.[10] A schematic of this is shown in Figure 1.5.

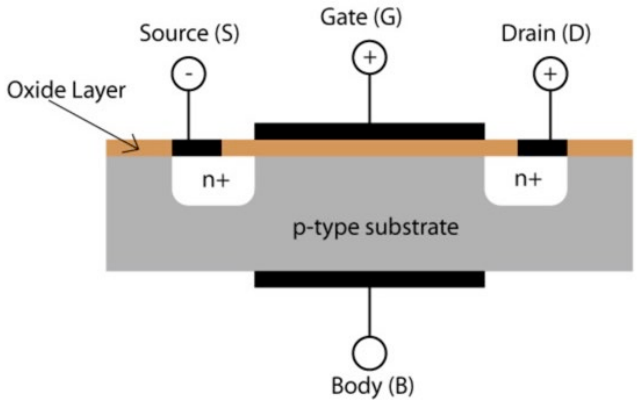

Figure1.5 MOSFET schematic9

Transistor devices typically have a specific voltage level that needs to be applied to turn them on such that current flows. When appropriate values of voltage are applied to the gate, an "inversion layer" forms which acts as a 2DEG.[10] At this voltage threshold the Fermi level in the very top layer of material drops below the actual Fermi level in the surrounding material and creates a region of mobile electrons. This is caused by the supplied voltage causing band bending in the valence and conduction bands.[10] This effectively confines the electrons to the interface between the semiconductor and the oxide. The band bending that occurs to form this inversion layer is shown in Figure 1.6b.

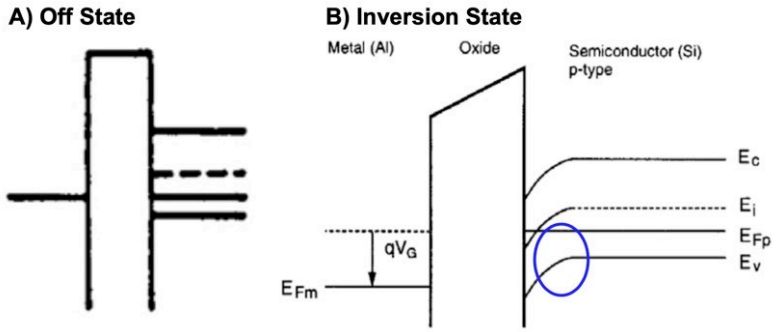

Figure 1.6 A) Flat band diagram for MOSFET without gate voltage supplied10 B) Band structure for MOSFET in inversion mode11

The blue circle in Figure 1.6b shows where the inversion occurs due to the band bending. On either side of this small region, the Fermi levels are not inverted which creates significant barriers. This creates a small quasi-triangular QW that confines electrons into a 2DEG. Conduction between source and drain can then occur and the transistor is in the ON state. When the gate voltage is below this specific value, the bands do not bend appropriately and therefore no 2DEG forms (Figure 1.6a). In this situation, conduction between source and drain cannot occur and the transistor is in the OFF state. These diagrams illustrate the central role that band structure plays in the operation of these devices.

We can also engineer the confinement of electrons into a 2DEG by using heterostructure band gap engineering. Recalling Figure 1.3 and the different heterostructure types, we can sandwich a thin layer of one semiconductor material within another. One such structure is shown below in Figure 1.7.

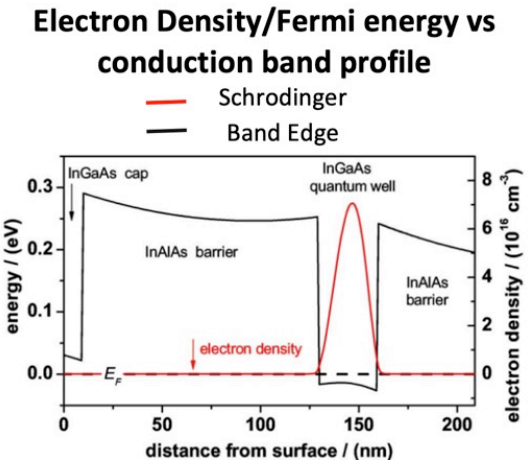

Figure 1.7 Band structure for a quantum well12

In the InGaAs QW, the CBM dips below the Fermi level which allows for the same type of quantum confinement in this device as was discussed for the MOSFET. Again, these large barriers in energy on either side of the quantum well effectively make the electrons stay in one physical place, the quantum well. The energies these electrons can have lie at certain values due to the quantum confinement of the electrons. The beauty of these QW-type heterostructures is that we can tailor these confined energy states by controlling the QW width via a traditional particle in a box model.[35]

One reason that QWs are so interesting is that when correctly designed, we can observe ballistic transport in the 2DEG. For high mobility materials at low temperature, the mean free path of the electrons can exceed the channel length and electrons travel through the channel without scattering.[10] Ballistic transport is not typically seen in bulk materials due to the many scattering mechanisms, but it is possible in 2DEGs where we can eliminate or minimize various scattering process of electrons in the QW.[14]

Ballistic transport in the absence of scattering enabled the first observation of the quantum Hall effect in 2DEGs. The classical Hall effect has been known about since the 1870s when it was discovered when a current is passed through a metal conductor in a

perpendicular magnetic field, charge builds up on one side. As the applied field is increased, the DC resistance in the direction of the current flow does not change but the resistance in the perpendicular direction increases linearly (Figure 1.8).[36]

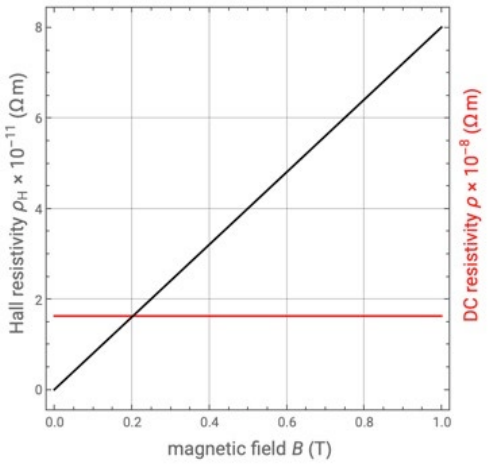

Figure 1.8 Classic Hall Effect13

The quantum Hall effect was first seen in the inversion layer of a Si MOSFET as described above, and has since been more deeply studied in GaAs/AlGaAs HEMTs and other semiconductor 2DEGs with sufficiently high mobility. [12,37,38] As the magnetic field is increased, a series of plateaus develop in the Hall resistance, with steps whose height is proportional to the resistance quantum e^2/h. [38] The DC resistance in the direction of the current flow develops a series of oscillations whose minima coincide with the plateaus in the Hall resistance indicating carrier transport without scattering.

In order to observe the quantum Hall effect, the material of interest must be cooled to very low temperatures to limit any phonon scattering mechanism that could occur. The material must also be subjected to a relatively high magnetic field as compared to the classic Hall effect.[38] This magnetic field will cause a current density to flow in the material, which will subsequently cause the electrons to move to one side of

the material and set up the classical Hall effect. The critical difference here from the classical Hall effect is that the material is bounded by energy barriers such that edge states exist which create interesting new properties. In the center of the channel, the electrons move in cyclotron orbits and have set radii as dictated by their quantum energies (Fig. 1.9a) (i)). These set orbital radii subsequently indicate the Landau levels. This occurs at the edges as well, but since the electrons are confined to the 2DEG region they cannot complete a full orbit and are therefore locked in 1D motion with electrons traveling in opposite directions at the two edges of the 2DEG (Fig. 1.9 a) (ii)).[14] An image of this is shown in Figure 1.9.

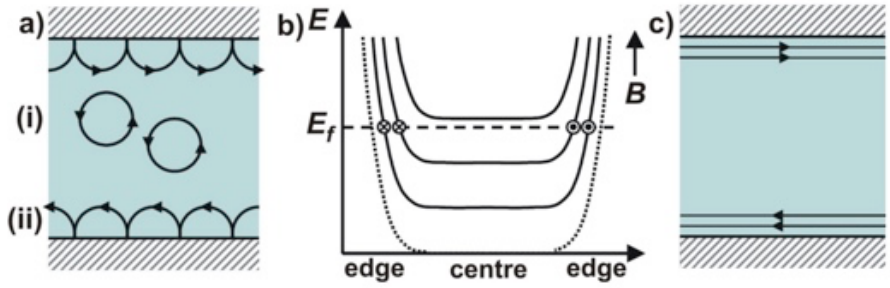

Figure 1.9 a) Electron cyclotron motion b) fermi energy across structure c) net effect on electron motion14

The Fermi energy of the material is strongly dependent on the magnetic field. By increasing the magnetic field strength, the Fermi energy level decreases, sweeping through the Landau levels to depopulate them.[14] As the Fermi energy level changes these edge states migrate closer to the center as the Fermi energy gets closer to crossing one of the Landau energy levels. When the Fermi energy crosses one of the Landau levels, the edge states meet in the middle of the quantum well and annihilate.[14]

This, in essence, sets up the Shubnikov-de Haas oscillations that are captured in the magnetoresistance measurements along the channel and are shown in Figure 1.10.

The peak of these oscillations occurs when these edge states collide because this causes significant scattering events not normally present. When the Fermi energy lies between Landau levels minimal scattering is present as the electrons are locked into 1D motion due to their orbital motion and phonon scattering is at a minimum. This sets up the troughs of the oscillations where the resistance is at a minimum due to the lack of scattering.[14]

The Hall plateaus that are seen transverse to the channel occur because they act as a measurement of the number of Landau levels present. When the Shubnikov-de Haas oscillations are at a minimum there is a plateau in the transverse measurement as the number of Landau levels is constant. As we increase the magnetic field and observe a peak in the Shubnikov-de Haas oscillations there is a step up in the transverse Hall resistance measurement of $h/\nu e^2$(where ν is the Landau level filling factor) since one of the 1D edge states has been removed from the channel. Both this longitudinal behavior and transverse behavior can be seen in Figure 1.10.

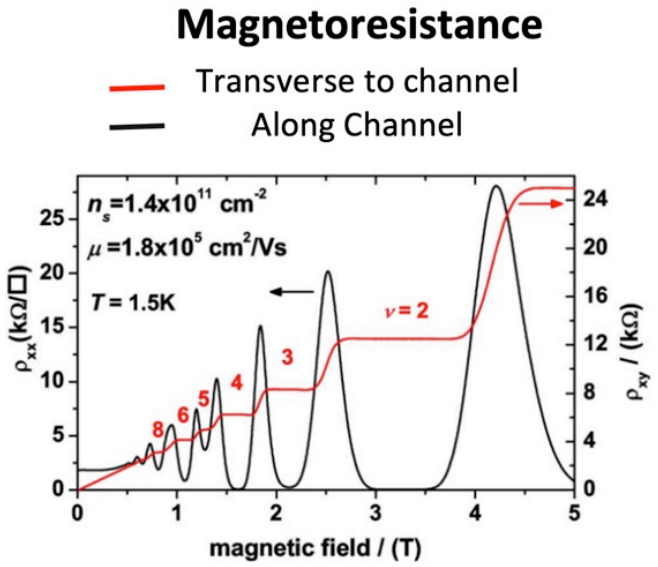

Figure 1.10 Quantum hall effect measurement with hall plateaus shown in red and Shubnikov-de Haas oscillations shown in black12

1.4 Interfacial Misfit Arrays

For the InAs/GaSb QWs that are of interest here, it is easiest to begin by using GaSb(001) substrates for the MBE growth. The homoepitaxial growth of GaSb barriers on a GaSb substrate poses significantly less challenge than growth on the highly lattice mismatched GaAs substrates we intend to adopt later in this research project. What is more, growth conditions for GaSb are well established for the (001) surface orientation, whereas growth conditions for GaSb with the unorthodox (111) orientation are much less well understood.

However, once we have learned to grow good quality InAs/GaSb QWs on GaSb(001) substrates, we will move to growing them on GaSb(111) substrates to see if we can also get good quality 2DEGs with this desirable surface orientation. The final step will be to see if we can then transfer the growths of these InAs/GaSb QW structures to (001)- and (111)-oriented GaAs substrates.

The focus of this work is to grow these structures of interest through molecular beam epitaxy or MBE. MBE is a thin film growth technique particularly beneficial for III-V semiconductor growth. MBE works by heating ultra-high purity elemental cells to create a vapor of atoms that are subsequently deposited on to a heated substrate. This allows for single crystal compound semiconductors to be formed. This technique is particularly beneficial due to the very abrupt interfaces that can be formed, the high level of control over doping density, and the low level of impurities that are imparted to the structures. This technique will be discussed in more detail in the methods section.

The previously stated issues of growing on GaSb substrates can be rectified by using GaAs substrates instead of GaSb substrates. The challenge come from the much

smaller lattice constant of GaAs (5.65Å) compared with GaSb (6.10Å). GaSb grown on a GaAs substrate will therefore experience large strains from the lattice mismatch of 8.0%. This difference is shown in Figure 1.4 above in the 6.1Å family section.

Interfacial misfit arrays (IMFs) have been established as an important tool for integrating two materials with significantly different lattice constants. Under normal circumstances, the strain resulting from heteroepitaxy of two highly mismatched materials will appear as threading dislocation defects that propagate up through the material. These defects degrade the overall material properties and will results in poorer electronic properties because they act as electron scattering centers. This is detrimental to the 2DEG system of interest here, as any carrier scattering will reduce the electron mobility and limit our ability to observe the subtle physics of the quantum Hall effect. To avoid these threading dislocation defects, an IMF can be used to relieve the strain to in plane dislocations. IMFs are a two-dimensional arrays of 90º misfit dislocations that lie in the plane of the interface, propagating laterally rather than vertically. In effect, this isolates the strain-relieving defects to the layer where they are formed and allows high quality material to be grown on top. IMFs form when a single bond at the GaSb/GaAs interface is skipped after a periodic number of bonds equal to the ratio between the two lattice constants. This is schematically shown in Figure 1.11.

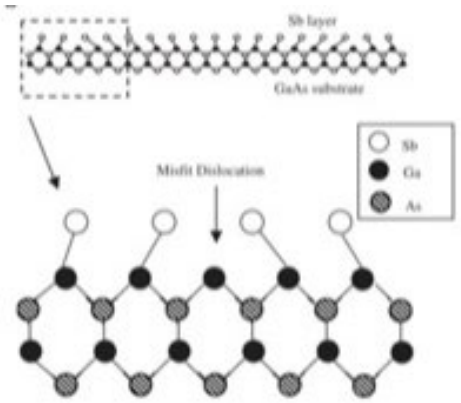

Figure 1.11 IMF bonding schematic15

1.5 Previous Work

While there has been previous work in the area of InAs/GaSb QW IMFs, much of it has been focused on the (001) substrate orientation. There are several papers investigating quantum effects in InAs/GaSb QW systems on GaSb (001) substrates. Additionally, IMFs of GaSb on GaAs have been reported since 1981[39] however the bulk of the work has focused on simply growing one material on top of the other. Eyink et al. grew an InAs/GaSb QW structure similar to that discussed in this thesis by creating an IMF to enable integration with GaAs(001) substrates and demonstrated good electronic and structural quality material.[3] This paper actually served as the basis for the structure used in the work disclosed in this thesis.

Ohtake et al. have studied GaSb growth on GaAs (111)A using thin InAs layers rather than an IMF structure with promising results as well. This group, however, did not focus on quantum well structures or electrical performance of the devices, just material quality as measured by XRD.[40] There are no current published papers concerning quantum well effects of a GaSb/InAs system grown on GaAs(111)A or IMF formation on GaAs(111)A.

CHAPTER TWO: EXPERIMENTAL METHODS

2.1 Molecular Beam Epitaxy

Molecular beam epitaxy or MBE is one method for thin film growth. While there are many techniques that exist to grow thin films, MBE stands out due to its ability to grow exceptionally pure, single crystal materials with exquisite control over layer thicknesses and atomically abrupt interfaces. It also has the ability to provide very fine control over doping density. MBE is carried out under ultra-high vacuum (on the order of 10 E-10 torr) which ensures extremely low levels of background impurities in the epitaxial film. A schematic for an MBE chamber is shown below in Figure 2.1. This three-chamber set up allows new substrates to be introduced to the system without exposing the growth chamber to atmosphere and breaking vacuum. This is very important to keep any impurities out of the growth chamber out and maintain ultra-high vacuum.

The substrates are mounted to molybdenum blocks by heating the block, melting indium on the block, and placing the substrate on the surface such that the backside gets coated and the indium adheres the two together. Substrates on their Mo blocks are placed in the intro chamber which is pumped down to ultra-high vacuum level. The substrates are then moved into the transition chamber which acts as a holding chamber. For our particular MBE system, six substrates can be loaded into the intro and transition chambers at a time. Then a single substrate is selected and moved into the growth chamber via the sample transfer mechanism.

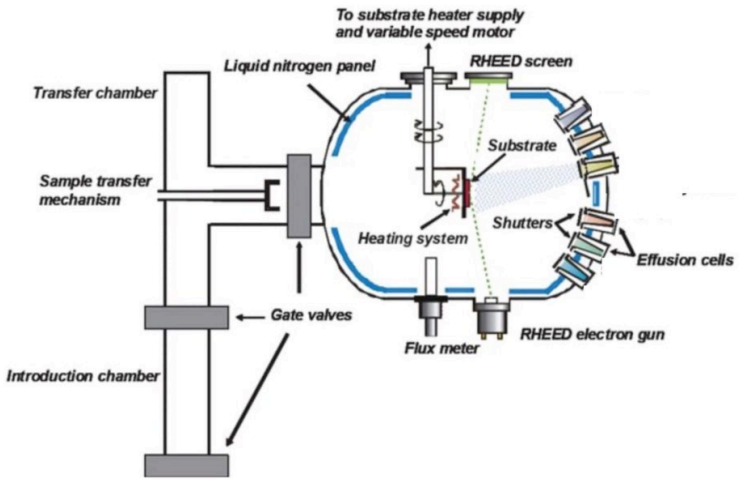

Figure 2.1 Schematic of an MBE chamber16

The growth chamber is surrounded by cryogenic panels that we can fill with liquid nitrogen. The cold surfaces of the cryopanels condense atoms within the growth chamber and hence reduce the pressure further. In the center is the substrate holder that we can heat and rotate during growth. Facing this are the effusion cells, each of which holds a single ultra-high purity element that serves as an ingredient for the materials we wish to grow. Each effusion cell can be heated to a range of temperatures to produce the desired growth rate of material. When heated, these cells create a vapor of atoms (group III elements) or molecules (group V elements). Opening a shutter in front of the cell allows this vapor to leave as a beam of atoms/molecules such that the beam is incident on the heated substrate. Near the substrate holder is a flux gauge which measures the flux of atoms (i.e. the number of atoms per unit area per unit time) leaving a given cell at some temperature, which can then correlate to the growth rate. We can directly measure the growth rate of a given material using reflection high energy electron diffraction or RHEED analysis; this process is described in further detail during the “RHEED” section.

The chamber must be cooled with liquid nitrogen for approximately two hours before growth to reach 77K and achieve the base pressure of the growth chamber (usually

10E-10 Torr range). The effusion cells are heated to the temperature corresponding to the desired growth rate and a substrate is loaded. The substrate must be heated to the deoxidation temperature as described in the RHEED chapter to remove the thermal oxide that acts as a protective coating for the substrate. This oxide protects the substrate from any impurities that could be introduced to the substrate from the time it is fabricated until it is used for growth. Compressed air-controlled shutters cover the effusion cells so that they are ready but atoms are not yet interacting with the substrate. When it is time to use a particular material, the shutter is opened so that the molecular beam lands on the substrate and the atoms can bond at appropriate sites on the substrate.

My research is focused on the growth of III-V materials. For III-V material growth the group V material shutter must be open from the start of substrate heating until the end of growth when the substrate is cooled back down. Group Vs have a higher vapor pressure and so tend to desorb from the heated substrate surface. Therefore, by having a constant excess overpressure of the group V material, we can replace the desorbing group V atoms while also providing enough for growth of the new atomic layers. If a group V material is not supplied when the sample/substrate is hot, droplets of the group III metal atoms will form on the substrate due to group V atom desorption, and the substrate becomes rough and unfit for sample growth.

When a sample is actually grown, atoms arrive at the surface and migrate around until they find a suitable bonding site. Initially when a new layer is starting to form, these atoms bond to only the layer below forming 2D islands. As more atoms arrive and a suitable number of islands have formed the atoms start bonding to the edges of the islands as well as to the layer below, and so the islands grow laterally. When the islands

have become large enough, they coalesce such that a new complete layer is formed. This process repeats to form a nicely layered crystal. Additionally, the atoms can bond to the step edges of layers that are forming. These atomistic processes are shown below in Figure 2.2.

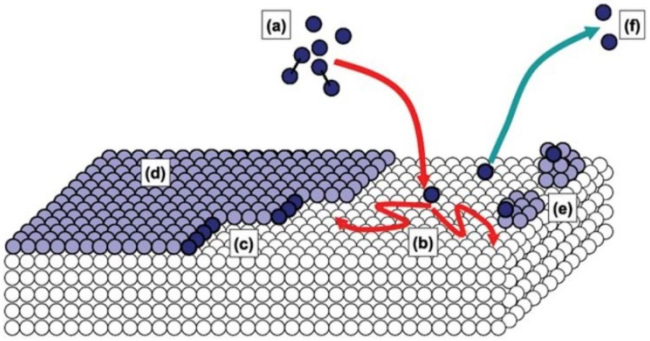

Figure 2.2 Atomic process occurring as a layer is formed A) atom arrives at the surface and adsorbs, B) atom diffuses across surface C) atom arrives at the step edge and forms step edge growth, D) atomic terraces formed through step edge growth E) island nucleation F) desorption of atom 16

2.2 Reflection High Energy Electron Diffraction

Reflection high energy electron diffraction, or RHEED, is one of the main in-situ process control tools available for MBE work. RHEED allows us to monitor the condition of the surface as growth is performed. RHEED works by shining an electron beam on the sample surface at an incident angle of just 2-3°. The electron beam is diffracted by the top few atomic layers of the sample surface and the diffraction pattern is reflected onto a phosphor screen and captured with a camera. This tool is first used to understand when the surface thermal oxide is removed. Initially, the RHEED shows a hazy pattern due to the amorphous structure of the oxide as shown in Figure 2.3a. As the substrate is heated to the deoxidation temperature for the material, the oxide evaporates and the RHEED can interact with the crystal. Due to the crystal nature of the substrate the RHEED pattern will change from a hazy pattern to a pattern of lines or spots. The

electrons are diffracting off the periodic structure of the crystal which allows for bright and dark spots that correspond to angles where the Bragg condition is met for the sample surface. There are many different patterns that can be seen in the RHEED depending on the crystalline structure of the material that is used. Some examples of these different patterns can be seen in Figure 2.3b and c. As growth occurs the nature and intensity of the RHEED pattern tells us whether the surface is atomically smooth or rough, and hence whether we are using the correct growth parameters. If the intensity begins to drop off significantly, it is a strong indication of a surface that is getting increasingly rough. Some natural fluctuations are to be expected, however a steep decline that remains low can be quite concerning. Additionally, as different materials are grown on a substrate the RHEED can transition to different patterns due to the different surface reconstructions of different materials, allowing the user to understand if the new material layer is forming as desired. The deoxidation (Figure 2.3(a)) vs clean surface (Figure 2.3 (b) and (c)) images for GaSb (111) substrate heterostructure growth as well as a schematic of the RHEED set up is shown in Figure 2.3.

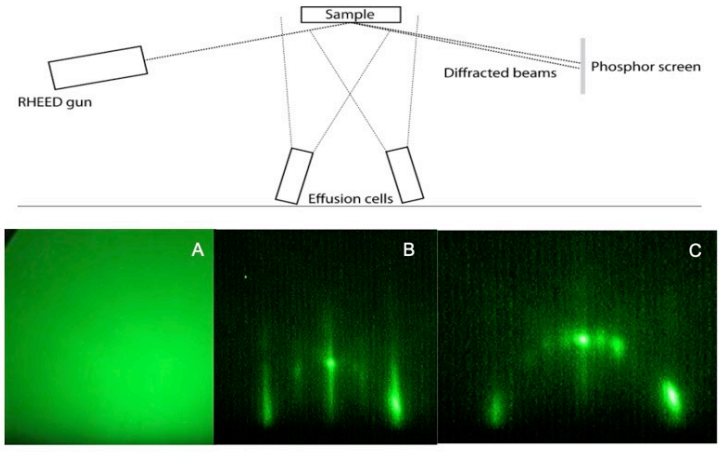

Figure 2.3 A schematic with the RHEED set up and sample stage17. A) a wafer with the thermal oxide present, B) a clean 2x pattern showing the oxide has been removed, C) and additional 5x pattern that can be seen as the sample is rotated

The RHEED is also the primary tool used to measure the growth rate of a material for a specific cell temperature. A specific method called RHEED intensity oscillations or RIOs is used. To do this, we monitor the intensity of one of the bright spots in the RHEED pattern under normal growth conditions (shown on the bottom right of Figure 2.4(a)). All growth is stopped and the surface is allowed to become smooth. Then we initiate sample growth and observe how the intensity of that diffraction spot varies. Smooth layer by layer growth produces oscillations in the RHEED intensity (see Figure 2.4(b)). The period of these oscillations corresponds to the growth of a complete monolayer of the crystal. If they are closer together, the material is grown faster, if they are further apart the material is grown more slowly. The reason for these oscillations is that as atoms arrive at the surface prior to bonding they migrate around and the surface is rougher which creates reduced intensity. When they bond at a specific site the surface becomes smoother creating peaks in the intensity. A schematic of this can be seen in Figure 2.4(c).

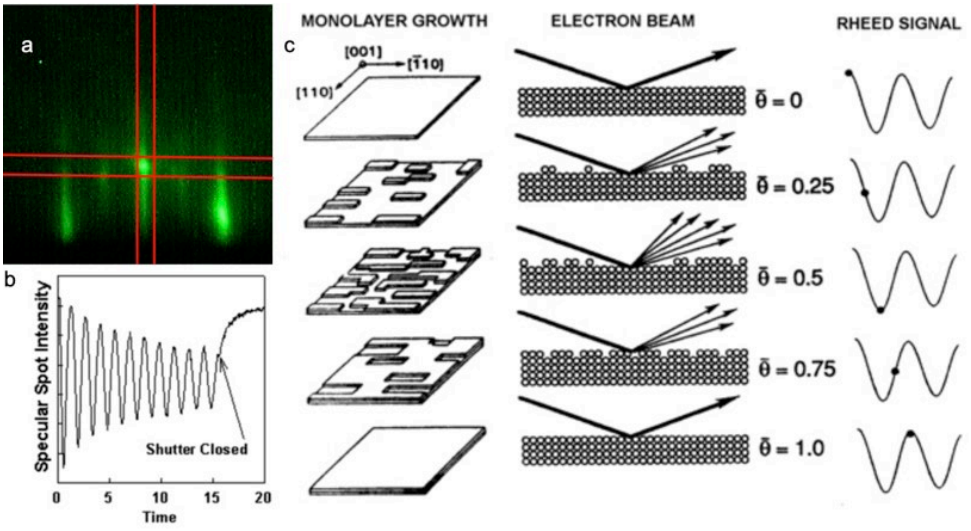

Figure 2.4 a) RHEED pattern with RIOs collection area highlighted, b) signal collected out of pattern area46 c) monolayer growth stage, surface schematic, and corresponding RIOs graph46

2.3 X-ray Diffraction

Following MBE growth, we use X-ray diffraction, or XRD to understand the composition of the material we have grown, how strained it is, and its crystallinity. These features can be determined from the location of the 2-theta-omega peak and the full width half maximum (FWHM) of the peak. The theoretical pure material 2-theta-omega value can be determined from Bragg's law given in equation 1. In this equation θ is the Bragg angle to be calculated, λ is the wavelength used in the XRD, d is the d spacing of the reciprocal lattice and n is the order of the diffraction peak.

$$n\lambda = 2dsin\theta \quad (1)$$

This tells the user the Bragg angle at which we should observe the diffraction peak for an unstrained film at pure composition. The width at half the maximum of the peak is used to determine how crystalline the film is. The broader the peak, the more disorder that is present in the crystal. XRD is accomplished by using X-rays since their wavelength is similar to that of the atomic spacing of the atoms in our crystals. As the X-rays bounce off the crystal structure, they create an interference pattern which can be read out. What is really being captured here is the spacing between the atomic planes which allows us to deduce the lattice constant of the material. Imperfections in the material will cause the diffraction pattern to change and therefore adjusts both the position and width of the peak that is measured. In order to analyze the films of interest, multiple calibration scans must be performed to compensate for the height difference due to indium mounting on the back of the sample as well as to adjust the detectors to the proper Bragg angle to scan across the peak where the 2-theta-omega condition lies.

In addition, for some sample types an additional rocking curve (omega) scan is performed when the dominant material grown is not the same as the substrate. This scan allows us to view both the major and minor axis of the ellipse that the material has in reciprocal space. The FWHM of the peak in the two directions tells us about the crystal quality of the heteroepitaxial film, where the narrower the rocking curve peak, the better the film quality. Figure 2.5 shows the difference between these two scans in reciprocal space, as well as a sample of the data.

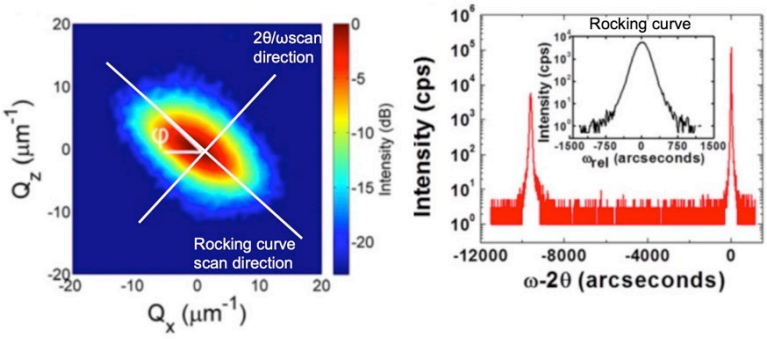

Figure2.5 Reciprocal space map for GaSb peak showing the difference between rocking curve and 2 theta scans, and a 2 theta scan with a rocking curve inset4

2.4 Atomic Force Microscopy

While XRD provides information about the crystal structure and composition of the material grown, atomic force microscopy or AFM provides information on the sample surface. AFM allows the user resolve differences in the height of the sample surface at the atomic level. This helps us understanding different dislocation type defects, surface roughness caused by these defects, and allows for the visualization of the atomic layers composing the crystal visible on the surface. AFM works by focusing a laser on a thin cantilever probe with a point on the bottom. As the probe moves across the surface it makes electromagnetic contact with the surface through weak van der Waals bonds. The minute deflections that are induced on the probe as a result of changing surface features

are monitored by how the laser beam deflection changes. These changes are then mapped to reconstruct the surface features. A schematic of this set up as well as a sample image that can be generated are shown in Figure 2.6. The sample image shows a heterostructure grown on GaSb(001). The layering seen in this image are the atomic layers of the crystal.

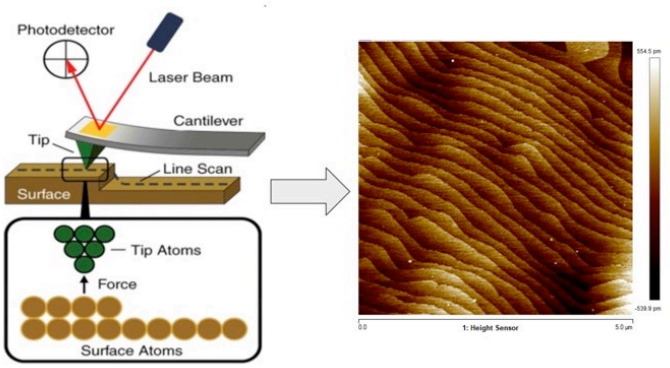

Figure 2.6 Schematic of how an AFM probe generates an image18 with a sample image taken from a GaSb surface

2.5 Transmission Electron Microscopy

Transmission electron microscopy, or TEM is a method that allows us to see details of a cross section of a sample with atomic level resolution. In order to perform TEM a cross section of the sample must first be taken. This is a destructive technique unlike many of the other characterization methods described here. This is accomplished by using a focused ion beam or FIB approach where a beam of ions is used to mill through the surface and create a cross sectional lamella. This lamella must be thinned so that it is thin enough for electrons to pass through. Once this sample preparation has been accomplished, an electron beam is passed through the sample which gets diffracted by the periodic structure of the crystal lattice. This diffraction pattern is collected and analyzed, allowing the user to visualize both the bulk sample structure and individual crystal planes. A schematic for the instrumentation of a TEM is shown in Figure 2.7.

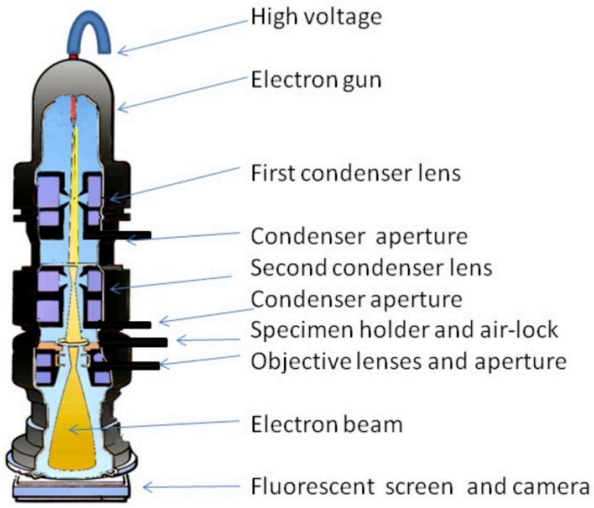

Figure2.7 Schematic of a TEM set up19

2.6 Scanning Transmission Electron Microscopy and Electron Energy Loss Spectroscopy

One additional mode available in the TEM set up is scanning transmission electron microscopy or STEM. In STEM the electron beam is focused to a narrower spot size and scanned across the sample to provide a higher level of resolution. STEM also allows for the use of electron energy loss spectroscopy or EELS. EELS is particularly useful because it allows one to map different elemental signatures as a function of their position in the STEM image, for example to visualize regions with different composition. In EELS we monitor the energy loss of the electrons as they pass through the sample. The electrons lose energy by interacting with the electrons of the sample material and the amount of energy they lose is different depending on the element that they interact with. EELS is particularly useful in monitoring whether or not the anticipated growth occurred as intended and if specific elemental species are confined to certain regions of the structure. A schematic of this instrumentation is shown in Figure 2.8.

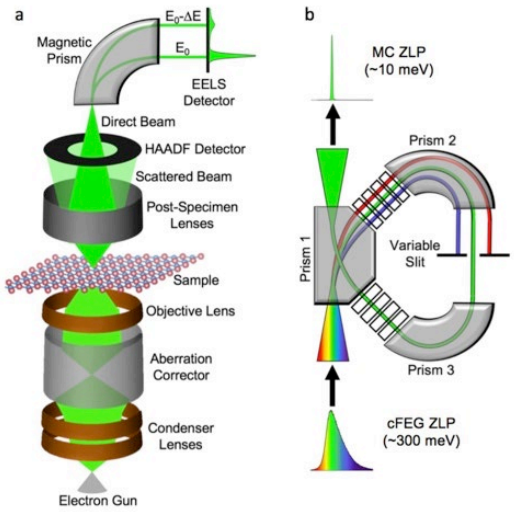

Figure 2.8 A schematic for a STEM (essentially the same as the TEM but containing the EELS equipment) B) schematic for EELS measurement20

2.7 Electron Channel Contrast Imaging

Electron channel contrast imaging, or ECCI is a mode of scanning electron microscopy or SEM imaging.[41] In SEM an electron beam is scanned across the sample and the scattered electrons are used to create the image. For ECCI the sample is specifically angled relative to the electron beam such that the crystallographic planes can diffract electrons which are collected.[42] Specifically, the back scattered electrons are used due to their penetration depth. They penetrate deeply enough that subsurface features can be resolved.[41] This allows for threading dislocations buried in the material to be imaged. ECCI allows us to quickly and nondestructively measure the total defect density at the surface of a given sample. While this data shows similar surface-level data as AFM does, it has the added advantage of also capturing some subsurface features and it provides larger area scans to obtain a better overall picture of material health. A schematic of this measurement can be seen in Figure 2.9 where 2.9a and 2.9b show the types of geometries that are possible and 2.9c and 2.9d are the types of images that are created by these different geometries.

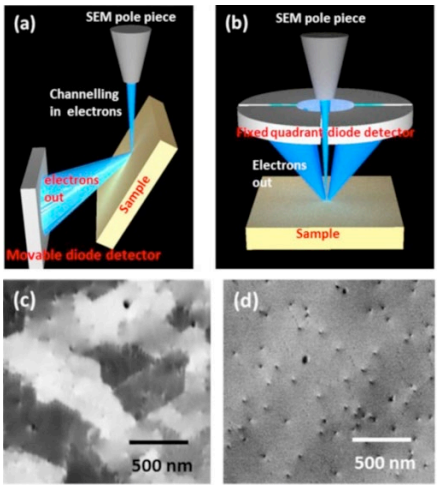

Figure 2.9 Schematic and image types for ECCI. A&B) types of geometry possible, C&D) types of images created21

2.8 Magnetoresistance Measurements

Magnetoresistance data is essential to studying quantum effects present in the 2DEGs at the center of this project. We pass a current along a thin channel containing the 2DEG, and measure the perpendicular (Hall) and longitudinal resistance as a function of applied magnetic field. These measurements take place at very low temperatures (usually 1-4K) although temperature may also be varied with transport features typically becoming less visible at high temperatures due to phonon scattering. The observance of Shubnikov-de Haas oscillations in the longitudinal resistance and plateaus in the Hall resistance are the signatures of the QHE. In effect, this technique allows us to evaluate our films for possible future applications and provides a read on the end quality of our material. An example of a magnetoresistance measurement is shown in Figure 2.10 for an InGaAs/InAlAs (001) 2DEG. This data was shown earlier but is replicated here for the sake of clarity.

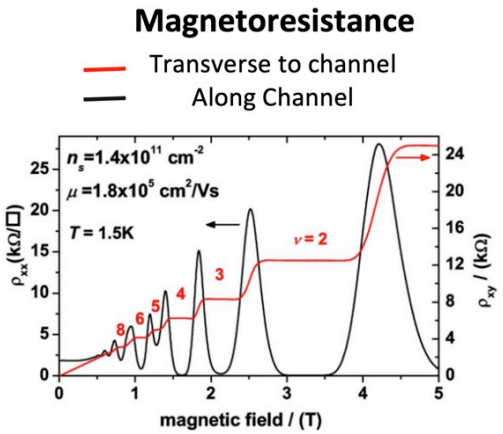

Figure 2.10 Quantum hall effect measurement with hall plateaus shown in red and Shubnikov-de Haas oscillations shown in black12

CHAPTER THREE: RESULTS AND DISCUSSION

3.1 General

The structure of interest for this project was based on a design by Eyink et al., [3] and focused on a 10nm InAs QW surrounded by GaSb barriers. To provide the free electrons to form the 2DEG a 10nm layer of n-doped GaSb was placed above the QW, separated by an intrinsic GaSb setback to minimize electron scattering from the ionized dopant atoms. We intentionally grew a single monolayer of InSb at the top surface of the InAs QW to prevent inadvertent GaAs formation. The full structure is shown in in Figure 3.1a. Band alignment simulation for this structure with both the (001) and (111) surface orientations were performed by our collaborator Dr. Carlos Cabrera-Perdomo at the University of Zacatecas. As Figure 3.1(b) shows, changing surface orientations has very little effect on the band structure.

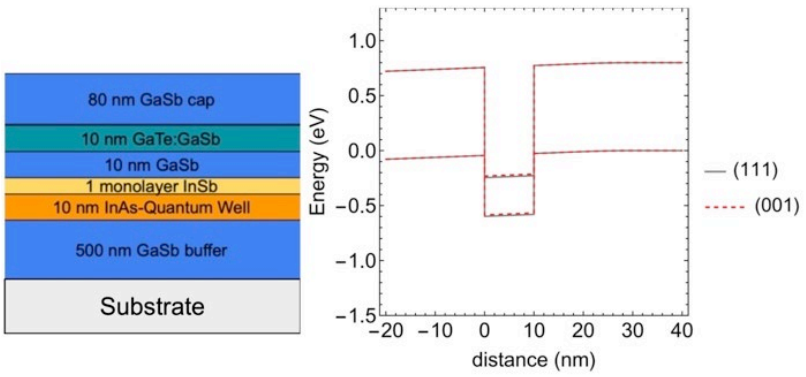

Figure 3.1 Sample structure and band alignment for this structure

3.2 InAs/GaSb QW samples grown on (001) substrate orientation

3.2.1 Growth on GaSb(001) substrates

The first step was to grow this structure directly onto a GaSb(001) substrate. Growth of InAs/GaSb(001) QW heterostructures is not itself novel, but it represents an important first step in ensuring that our growth conditions are dialed in correctly for later, more challenging aspects of this project. To accomplish this, we used a substrate temperature of 500°C for the GaSb growth with an Sb_2 flux of 2.6E-6 Torr, and a Ga growth rate of 0.3ML/s. For the InAs QW we reduced the substrate temperature to 400°C due to InAs requiring a lower temperature for optimum growth. The InAs growth rate was 0.5ML/s with an As_2 flux of 2.5E-6 Torr. The Te density in the n-doped GaSb layer was set to be 2E18 cm^{-3}. Our first attempt at this growth did not have sufficient doping. We therefore reran the n-doping calibration using a Van der Pau measurement and then regrew the structure with our corrected Te doping.

Once this structure was grown, we characterized it using AFM and XRD. The results from the AFM can be seen in Figure 3.2. A large area 50 × 50μm^2 scan was performed in addition to 5 × 5 μm^2, 2 × 2μm^2, and 1 × 1μm^2 scans. Figure 3.2a shows the 50×50μm^2 scan. This scan is dominantly performed as a defect scan. This allows us to see the general health of the material. From this image we can note that there are some trapezoidal surface features (height ~1.7nm, diameter ~ 1.3 μm) that may form in the vicinity of threading dislocations that propagate up through the material. However, their density is relatively low (~0.052/μm^2) and there are large regions of healthy material between these defects. The rms roughness (Rq) of this sample averaged over 50 × 50 μm^2

was 4.99Å, indicating an acceptably smooth surface for these InAs/GaSb(001) QW samples.

Figure 3.2b shows the equivalent 2 × 2 μm^2 scan from this sample. We perform this scan to get a sense for the growth mode of the material and to see the surface morphology in more detail. In this image we can resolve atomically high surface with rectangular islands forming on the terraces, suggesting a growth mode on the boundary between layer-by-layer and step-flow growth. Rq for Fig 3.2b was 1.08 Å.

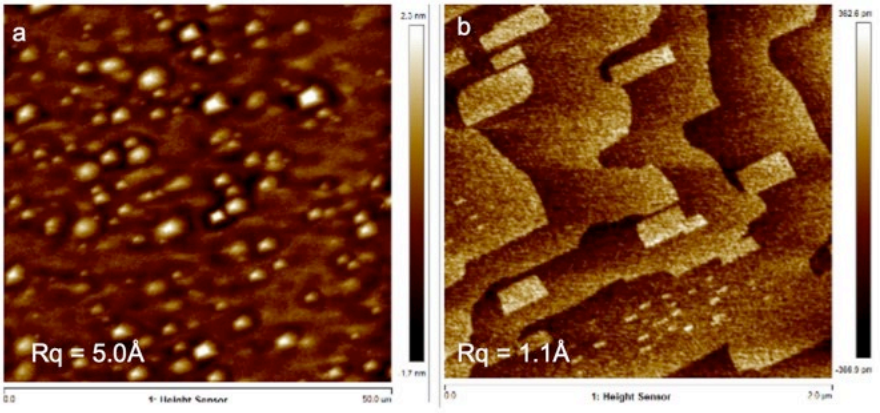

Figure 3.2 a) 50x50 □m2 scan with Rq =5.0Å. b) 2x2□m2 scan with Rq = 1.1Å

In addition to the AFM, XRD was performed to assess the crystal quality (Figure 3.3). This is a 2θ/ω scan performed with GaSb(004) Bragg conditions of 60.7226°. The FWHM for this peak is 199.5" which indicates good material quality.

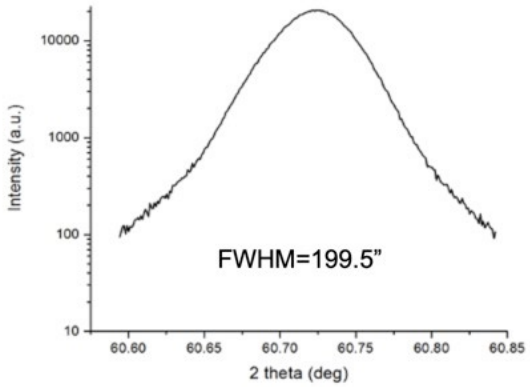

Figure 3.3 XRD 2theta omega scan with FWHM of 199.5”

Based on these XRD and AFM results, we can conclude that using our chosen MBE conditions, we can grow high quality InAs/GaSb QW samples on GaSb(001) substrates, and further optimization was not needed for this proof of concept project stage.

Our collaborators at INL then performed magnetoresistance measurements to look for evidence of the quantum Hall effect in the 2DEGs we expect to form in these InAs/GaSb(001) QWs. Figure 3.4 shows that Shubnikov-de Hass oscillations in the longitudinal resistance of the 2DEG as the magnetic field is swept, which is consistent with transport in the topologically protected edge states of the quantum Hall effect. These oscillations can be seen up to 20 K, a surprisingly high temperature, which suggests that these edge states are well protected against phonon scattering. When the temperature was increased to 100 K however, the oscillations disappeared due to increased phonon scattering. We note that the resistance in the troughs of these oscillations does not reach zero as it would in an ideal 2DEG, due perhaps to scattering from defects or suggesting parallel conduction is present in the sample, possibly in the n-doped GaSb layer or simply due to the fact that the undoped GaSb substrate is intrinsically conductive.

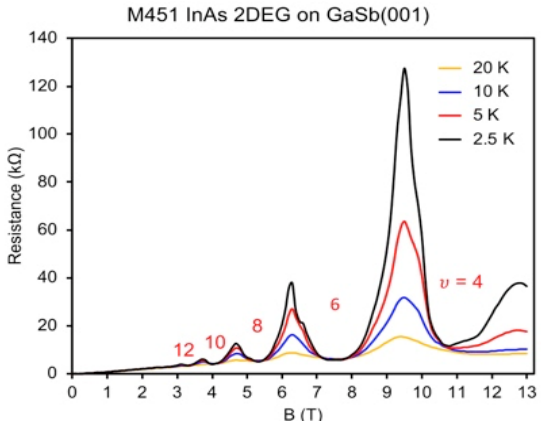

Figure 3.4 Longitudinal magnetoresistance measurements performed at INL showing Shubnikov-de Haas oscillations resolvable up to 20K

Corresponding measurements of the Hall resistance as a function of applied magnetic field have not yet been completed but we anticipate seeing the plateaus of the quantum Hall effect in those measurements.

3.2.2 Growth on GaAs(001) substrates

The next stage in the experimental work was to port the InAs/GaSb QW structure and growth conditions developed above to the GaAs substrates we are targeting in this project. As previously described, we used an IMF technique to purge excess As from the GaAs surface and replace it with Sb, prior to growth of the heteroepitaxial GaSb buffer. If grown correctly, the in-plane misfit array relieves the strain at the GaSb/GaAs interface due to lattice constant mismatch, such that high quality material can be grown above. To do this, first 100 nm of GaAs is grown at 580°C substrate temperature and with a growth rate of 0.3ML/s and with a flux for the arsenic of 2.5E-6 Torr. Once this initial GaAs layer is grown, the Ga shutter is closed for 10s, and the Sb valve is opened to the value that provides the adequate flux for the growth. Note that during this step, the Sb shutter remains closed so that no Sb atoms can reach the substrate surface. Next the As valve is closed down and there is a 10s pause, followed by closing the As shutter with a 5s wait.

Then we introduce a further 10s pause, which is long enough for the excess As adatoms to leave the sample surface, but not so long that As begins to desorb from the GaAs and leave behind Ga droplets that would destroy the surface. After this pause, we open the Sb shutter for a 3 min soak to ensure that the surface is Sb-terminated rather than As-terminated.[43] This soak time is performed while the material is cooled from 580°C to 500°C such that the material is at the proper temperature for GaSb growth when the soak is completed. We should note that we tried to carry out the switch from As to Sb based on well-established RHEED transitions for the As- and Sb-terminated surfaces[4,43]. However, we found that because in our group we indium mount our substrates to molybdenum blocks with high thermal mass these transitions occurred too slowly for us to observe. As a result, we used the timed approach described above for all subsequent GaSb/GaAs IMF growths.

Once the sample has been cooled to 500°C, we initiate growth of the GaSb to form the IMF. We use the same MBE growth conditions here as those described above for the growth of homoepitaxial GaSb directly on GaSb(001). Initially the GaSb forms 3D islands on the surface which we observe as the appearance of a spotty pattern in the RHEED. However, after we have grown ~25 nm of GaSb, the RHEED pattern becomes streak again, indicating that the sample surface has smoothed back out.

Following growth of the full InAs/GaSb QW structure on top of the GaSb/GaAs(001) IMF, we performed AFM to explore the resulting surface morphology. The same set of scans was performed on this sample as were performed on the GaSb(001) substrate sample. The $50 \times 50 \mu m^2$ scan and the $2 \times 2 \mu m^2$ scan are shown in Figure 3.5a and b respectively. Figure 3.5a again shows that the surface is covered in

trapezoidal islands which is common for IMFs[3]. Compared to the surface of the GaSb(001) substrate sample these defects are smaller in diameter with a larger height (diameter ~ 1.122 μm, height ~ 3.464 nm), but much higher in density (0.372/μm^2). For this image, Rq = 1.44nm, roughly three times larger than the 0.499nm measured for the GaSb(001) substrate sample surface in Figure 3.2a, but still showing reasonable material quality.

The high density of these defects made it impossible to find a region without them to gauge only the atomic layer health. The 2 × 2 μm^2 scan shown in Figure 3.5b shows a closer view of these islands where we can clearly resolve atomic steps on the sides of the islands. A close-up view of the tops of these islands inset to figure 3.5c reveals their spiral structure (see inset), suggesting that these surface features are associated with a screw-type dislocation which is expected for this IMF.

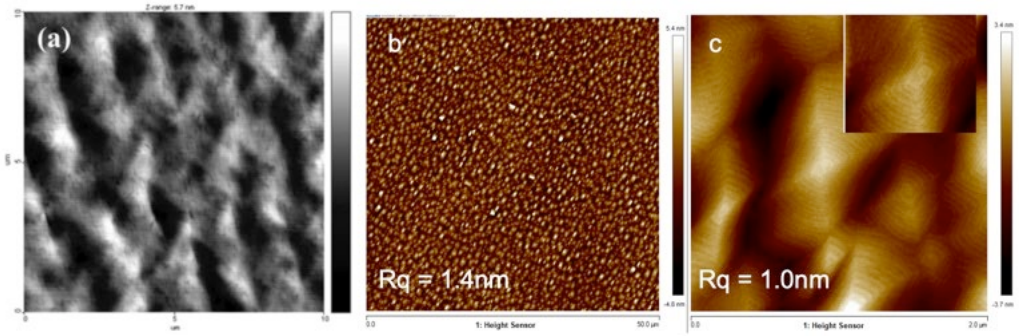

Figure 3.5 a) reference image from the literature[3] b) 50 × 50 μm^2 scan , Rq = 1.4 nm c) 2 × 2 μm^2 scan, Rq = 1.0 nm with inset of peak of defect

XRD was also performed to understand the crystal quality (Figure 3.6). The 2θ/ω scan was performed with the Bragg conditions for GaAs(004) of 66.07°. The scan was performed over a wider range such that the GaSb peak was also captured in this scan. The GaSb(004) Bragg angle is 60.7226°. From the 2θ/ω scan both peaks lie nominally where

they should indicate minimal strain in the material. The FWHM of the GaSb peak on the 2θ/ω scan is 228.3” showing reasonable material health.

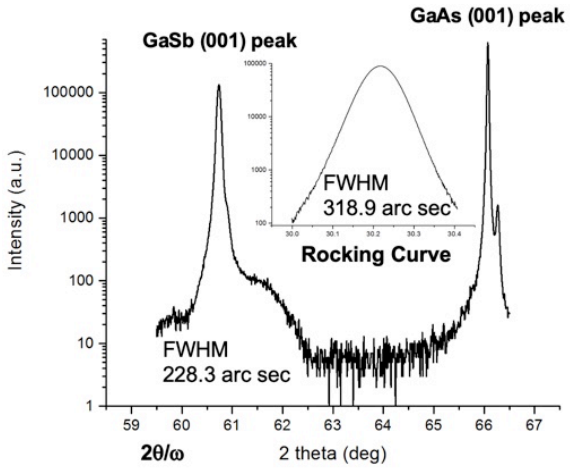

Figure 3.6 2 θ/ω XRD with GaSb(001) peak FWHM of 228.3”. Inset shows rocking curve scan or the GaSb peak with FWHM of 318.9”.

We also performed a rocking curve (omega) scan on the GaSb(001) peak, the FWHM of which provides information about the quality of the IMF-based GaSb material (inset to the 2θ/ω scan). For the rocking curve scan the Bragg conditions are changed to the GaSb(004) condition previously stated. The FWHM of the peak here is 318.9” which is relatively high but still shows reasonable material quality. The current best reported value for a similar structure is 240”. [4]

In summary, both AFM and XRD show that we can grow InAs/GaSb QW samples on top of the GaSb/GaAs(001) IMF interfaces with reasonable quality. The samples grown at BSU are similar to those reported in literature [3,4] with slightly reduced quality. The resulting InAs/GaSb(001) IMF-based QW samples have been sent to INL for magnetoresistance measurements. We are awaiting the results, which will allow us to compare the 2DEGs formed on GaSb(001) and GaAs(001) substrates to gauge the effect of the IMF and associated defects on electron transport.

3.3 InAs/GaSb QW samples grown on (111)A substrate orientation

3.3.1 Growth on GaSb(111)A substrates

After demonstrating InAs/GaSb QW growth on both GASb(001) and GaAs(001) substates, the next goal was to establish the MBE conditions needed to grow this same structure on GaSb(111)A substrates. MBE growth on GaSb(111)A surface is significantly less explored than for GaSb(001) and so finding the optimal growth conditions is not a trivial problem. We first tried the same growth conditions we used for growth on the GaSb(001) orientation (GaSb growth rate = 0.3ML/s, Sb_2 flux = 2.8E-6 Torr) but found that the surface was rough with an extremely high density of triangular pyramidal features that mirror the threefold symmetry of the GaSb(111)A substrate (Figure 3.7a). These features are typical for unoptimized growth on (111)-oriented substrates and stem from the fact that the sticking coefficient of the group V atoms is much less on the (111)A surface than the (001) surface.[2]

We therefore explored changes to the MBE conditions that would provide a higher V/III flux ratio, to ensure that there is sufficient Sb to compensate for the lower sticking coefficient. We therefore reduced the growth rate from 0.3ML/s to 0.13ML/s, and increased the Sb_2 flux to 4E-6 Torr. The result was a dramatic reduction in the areal density of the triangular features with smooth regions in between (Rq = 3.83nm) (Figure 3.7b). The areal density in Fig 3.7a is 0.09/μm^2, in Fig 3.7b the areal density is 0.05/μm^2, and in Fig 3.7c the areal density is 0.01/μm^2. After exploring a variety of growth conditions we found that we obtained the highest quality surfaces with Rq = 3.14nm for the lower growth rate of 0.13ML/s with an intermediate Sb_2 flux of 3E-6 Torr (Figure 3.7c).

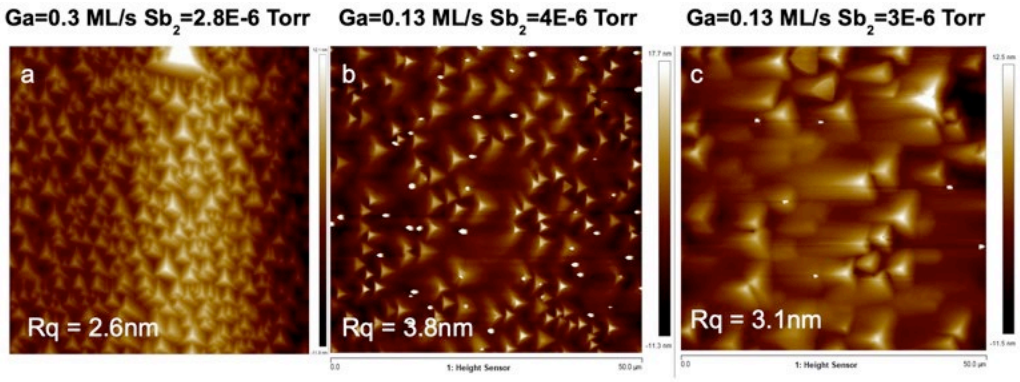

Figure 3.7 50x50μm^2 scans for A) Ga growth rate=0.3ML/s, Sb flux=2.8E-6, rq=2.59 nm , B) Ga growth rate=0.13 ML/s, Sb flux=4E-6, rq=3.83nm , C) Ga growth rate=0.13 ML/s, Sb flux=3E-6, rq=3.14nm

Although the lower growth rate significantly increases the time required to grow the InAs/GaSb QW sample, the final surface morphologies were comparable to the equivalent samples grown on GaSb(001) substrates (Figure 3.2).

Small area 2 ×2 μm^2 scans of these samples are shown in Figure 3.8, mirroring the trends observed in the large area scans shown above. The biggest impact on the surface morphology comes from the large reduction in the density of the triangular islands when the GaSb growth rate is reduced. At this lower growth rate, changing the Sb_2 flux has a weaker effect on sample morphology with both samples showing nice periodic surface steps with wide atomically smooth terraces. When compared with the sample grown under an Sb_2 flux of 4E-6 Torr (Rq = 1.44Å) (Figure 3.8b), an Sb_2 flux of 3E-6 Torr produces a surface with narrower terraces and a slightly lower Rq value of 1.23Å (Figure 3.8c).

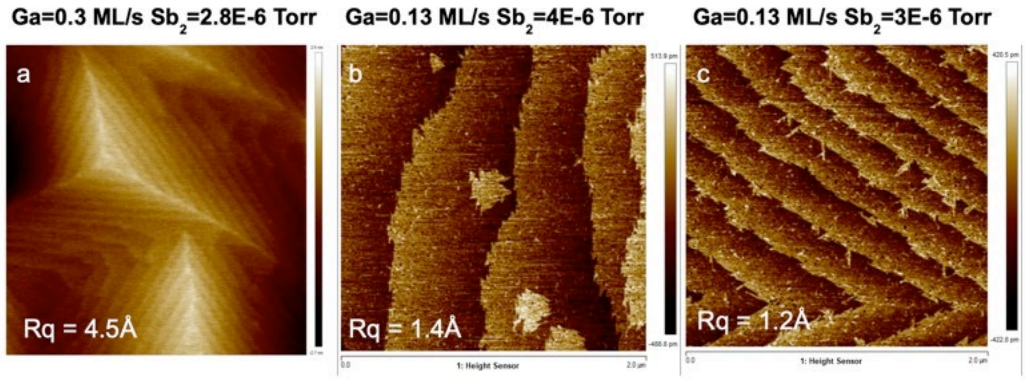

Figure 3.8 2x2μm^2 scans for A) Ga growth rate=0.3ML/s, Sb flux=2.8E-6, rq=0.452nm , B) Ga growth rate=0.13 ML/s, Sb flux=4E-6, rq=0.144nm , C) Ga growth rate=0.13 ML/s, Sb flux=3E-6, rq=0.123nm

XRD scans from the same set of experiments are shown in Figure 3.9. These scans were performed at the GaSb (111) Bragg condition of 25.285º. These results show much more clearly how the Sb flux change has affected the material. The FWHM of the GaSb peak for the sample grown at high growth rate (125.6") is actually narrower than for the sample grown at lower GaSb growth rate with high Sb_2 flux (168.5"). The sample grown at the lower GaSb growth rate with the intermediate 3E-6 Torr Sb_2 flux again shows the best material quality with FWHM 75.9". This is the opposite of what was captured in the AFM where the change in GaSb growth rate had the biggest impact on material quality improvement, while the two Sb_2 fluxes that were used looked relatively similar.

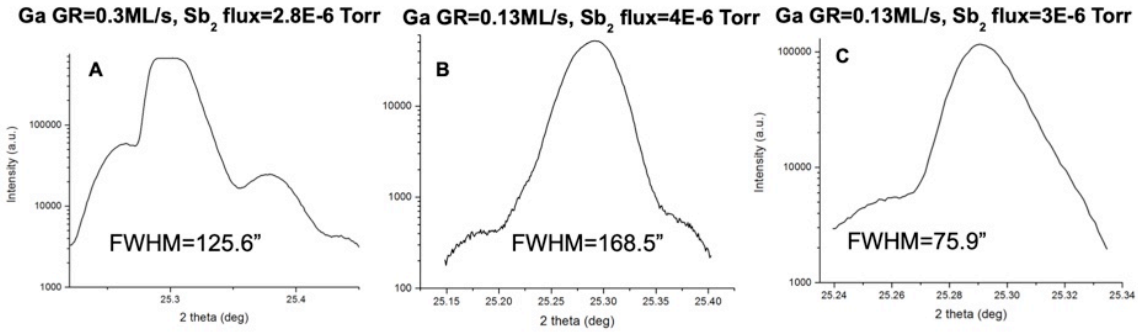

Figure 3.9 XRD 2θ/ω scans for A) GaSb growth rate=0.3ML/s, Sb flux=2.8E-6 Torr, FWHM=125.6", B) GaSb growth rate=0.13 ML/s, Sb flux=4E-6 Torr, FWHM=168.5", C) GaSb growth rate=0.13 ML/s, Sb flux=3E-6 Torr, FWHM=75.9".

By combining the AFM and XRD results it is clear that the GaSb growth rate of 0.13 ML/s and the Sb_2 flux of 3E-6 Torr provide the best results for growth on InAs/GaSb QWs on GaSb(111)A substrates. This best sample has been sent to INL for magnetoresistance characterization and we are awaiting the results.

3.3.2 Growth on GaAs(111)A substrates

The final project stage was to take what we had learned from growth on the other three substrate types and transfer it to grow the InAs/GaSb QWs on GaAs(111)A substrates via a modified IMF approach. For growth of the InAs/GaSb QW sample itself we used the same growth conditions that we optimized for the GaSb(111)A substrates.

Growth of a GaSb/GaAs(111)A heteroepitaxial interface however represented an entirely novel research direction as IMF-formation has only been explored on (001)-oriented samples to date. The first step was to optimize the growth of homoepitaxial GaAs buffers on GaAs(111)A substrates so as to provide a smooth high-quality starting surface upon which to form the GaSb IMF. To do this we grew a few samples of 250 nm of GaAs on GaAs(111)A substrates and found that a GaAs growth rate of 0.406 ML/s

with an As_2 flux of 1E-5 Torr and a substrate temperature of 580°C produced the best quality GaAs surfaces.

From here were proceeded with the first experiments to explore IMF formation at a GaSb/GaAs(111)A interface. We began by exploring the effect of the Sb_2 flux used for the entire growth (the soak time and the growth time). We grew the InAs/GaSb QW structure of interest at 2E-6, 3E-6, and 4E-6 Torr Sb_2 flux values. Again, these were assessed using the same set of AFM scans, however we performed 80 × 80μm^2 scans for these experiments rather than 50 × 50μm^2 scans. We wanted to see if this additional area provided any further detail about the samples, which it did not so after this set of experiments we returned to our typical 50 × 50μm^2 scans. These results can be seen in Figure 3.10, however the large area scan was missed on the 2E-6 flux sample.

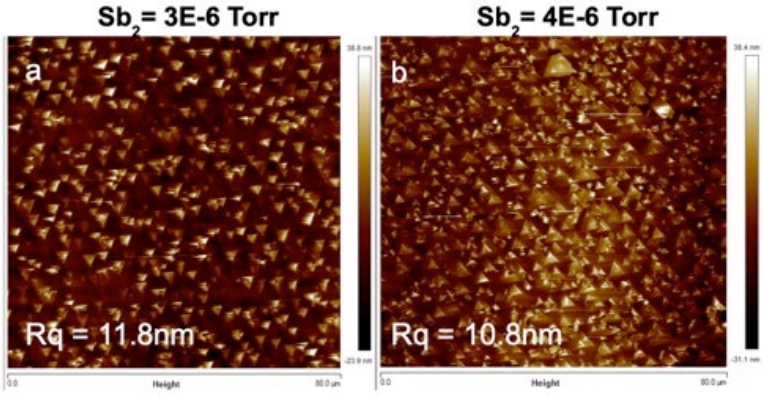

Figure 3.10 80x80 μm^2 AFM scans A) 3E-6 SbTorr flux, rq= 11.8nm , B) 4E-6 Sb Torr flux, rq=10.8nm

These results indicate that although the 3E-6 Torr flux produced a lower density of the triangle defects than the 4E-6 Torr flux, they appear to be larger as indicated by the higher Rq value for this sample; 11.8nm compared to 10.8 nm for the 4E-6 Torr flux sample. The smaller area 2 × 2 μm^2 scans show similar results, which are shown in

Figure 3.11. The 2E-6 Torr flux sample has such high defectivity that even for these small area images the defectivity is too high to identify the atomic layering. Although this sample is smoother than the 3E-6 Torr sample, the overall quality of the material is much lower, with atomic layering visible on the 3E-6 Torr sample. The 4E-6 Torr sample shows the best overall quality with a roughness value of 1.69nm, a value that may in fact be higher for this particular image due to the feature in the top right. We see no evidence of the spiral-type defects observed for the GaSb/GaAs IMF samples grown on GaAs(001).

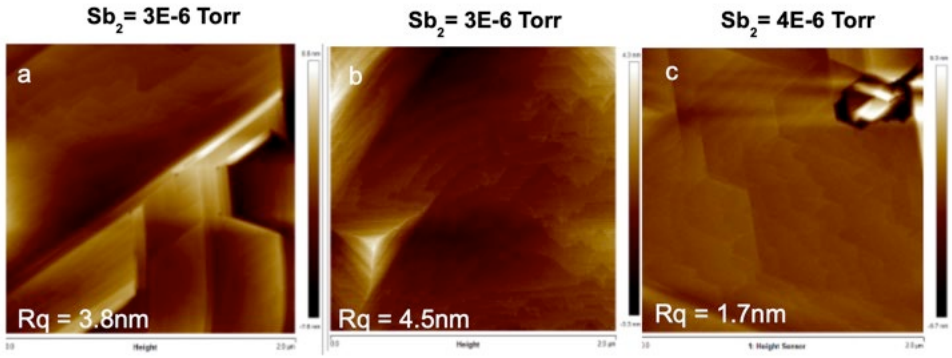

Figure 3.11 2x2 μm² AFM scans A) 2E-6 Sb Torr flux, rq= 3.8nm , B) 3E-6 Sb Torr flux, rq= 4.5nm C) 4E-6 Sb Torr flux, rq=1.69nm

To back up these results we also did XRD (Figure 3.12). For this we used GaAs(111) Bragg conditions of 27.3079° for the 2 theta scan and GaSb(111) Bragg conditions for the rocking curve (omega) scan matched to the values stated in the GaSb(111) substrate section. As for the (001)-oriented IMF samples, we see two peaks- one from the GaAs substrate and the other from the GaSb grown above the IMF.

These data show that the sample grown with an Sb_2 flux of 4E-6 Torr has the narrowest FWHM in the rocking curve scan suggesting the best material quality. Indeed, the GaSb peak in the 2θ/ω scan reveals thickness fringes indicative of an extremely flat

GaSb/GaAs interface. The rocking curve FWHM is 124.7", which is significantly lower than the best reported value in the literature of 240" for GaSb grown on GaAs(001) by this IMF technique.[4] For comparison FWHM the value for the 2E-6 Torr and 3E-6 Torr samples are 353.2" and 498.6" respectively. The data conclusively indicates that a high Sb_2 flux of 4E-6 Torr is needed to grow good quality GaSb/GaAs IMF samples. It is also worth noting that the intensity of the GaSb peak for the 4E-6 Torr sample is an order of magnitude higher than for the other two samples which also suggests excellent material quality. For the best sample we can asses the GaSb peak location in the 2θ/ω scan to understand the strain. When the GaAs peak in 3.12c is normalized to its Bragg angle the peak position of the GaSb is located at 25.27° indicating that the film is >99.9% relaxed. This is comparable to state of the art GaSb(001) IMFs.[4]

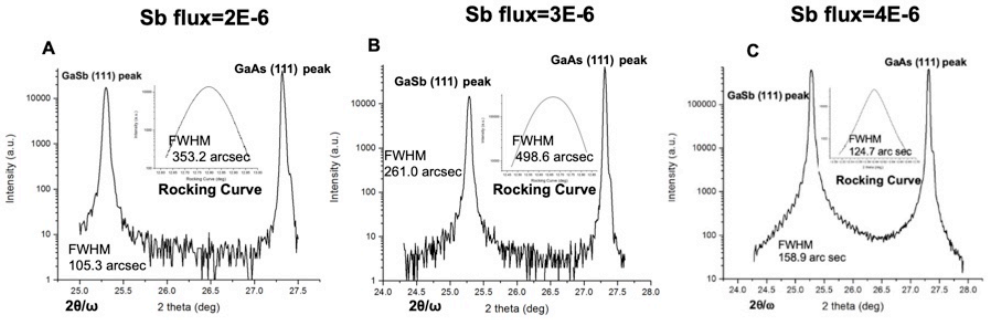

Figure 3.12 XRD 2θ/ω scans with rocking curve inset A) 2E-6 Sb Torr flux, FWHM=353.2" , B) 3E-6 Sb Torr flux, FWHM= 498.6" C) 4E-6 Sb Torr flux, FWHM=124.7"

By assessing both the AFM and the XRD, the data clearly show that overall a flux of 4E-6 Torr provides the best material quality for the growth of InAs/GaSb QWs via IMF arrays on GaAs(111)A substrates. In addition to the Sb_2 flux, other MBE parameters of interest include GaSb growth rate and substrate temperature. Since the growth rate was already at 0.13 ML/s, reducing it further was not practical for the growth of thick samples

needed in this project. The optimal substate temperature for growth of GaSb(111)A was shown to be 500°C in a series of experiments carried out by another member of our lab.[44]

Since our material quality appeared reasonable following AFM and XRD, we sent these samples to our collaborators at Stanford for ECCI measurements (Figure 3.13 and 3.14). ECCI is a SEM-based technique that is extremely sensitive to the presence of defects, such as threading dislocations, allowing us to calculate the threading dislocation density (TDD) for these samples, an important figure of merit for highly mismatched samples such as these.

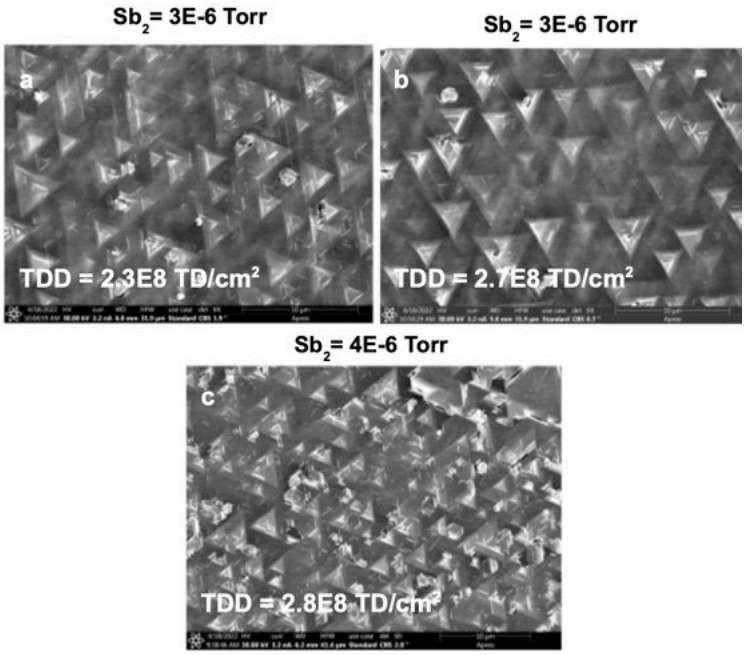

Figure 3.13 ECCI scans A) 2E-6 Sb Torr flux, TDD=2.3E8 , B) 3E-6 Sb Torr flux, TDD= 2.7E8 C) 4E-6 Sb Torr flux, TDD=2.8E8

These images show that the TDD is actually lowest on the lowest Sb flux and highest for the highest Sb flux converse to what the XRD showed. The defects themselves appear to be smaller in the highest Sb flux image with the 2E-6 and 3E-6 flux images showing roughly comparable sizes. The small white lines that appear in these

images are likely plane defects and are not visible in the AFM. These white lines appear to be oriented along the edges of the triangles.

ECCI measurements performed in out of channeling condition show large cracks are present in these samples (Figure 3.14), the number of which increases as we increase the Sb_2 flux. These defects appear to land directly on top of the large triangle defects and are likely the results of a significant amount of strain building up at these locations. Since the 4E-6 flux sample has a higher density of these triangular defects, it makes sense that it would have a more of these cracks, despite the defects being smaller.

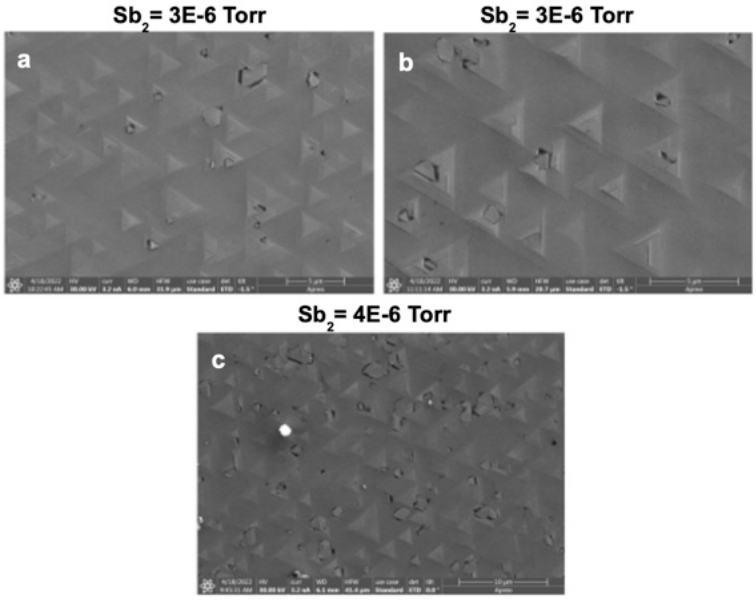

Figure 3.14 ECCI out of channeling scans A) 2E-6 Sb Torr flux, B) 3E-6 Sb Torr flux C) 4E-6 Sb Torr flux

In addition to these crack-type defects, the same white lines that were visible in the first ECCI presented are visible on the 3E-6 flux sample which indicates they are most severe on this sample. No TDD counts were available for this image type.

Based on the XRD we sent the 4E-6 flux sample for TEM analysis. This was performed in both high-quality regions of the samples as well as areas beneath the

triangular defects to gain a deeper understanding of what was occurring and causing these defects. Figure 3.15 shows a large defect free region corresponding to a smooth area of the sample between the triangular defects. The lack of threading dislocations or other extended defects in the GaSb(111)A shows that the array of in-plane misfit dislocations that make up the IMF have efficiently relieved the large compressive strain at the GaSb/GaAs interface without the nucleation and glide of threading dislocations. The InAs(111)A QW is continuous and uniform across the width of the imaged region, which is very promising for studies of the 2DEG in these samples.

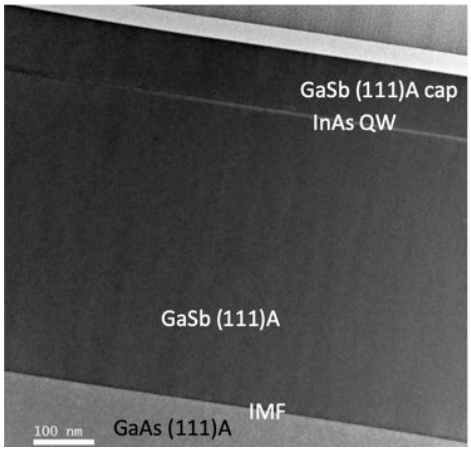

Figure 3.15 TEM of large defect free region performed on 4E-6 Torr sample

As we collect TEM images at higher magnification, we gain more information about the IMF (Figure 3.16a). These images reveal periodic dark spots at the GaSb/GaAs(111)A interface. Fast Fourier transform filtering of the TEM images allows us to clearly resolve the misfit array of the IMF (Figure 3.16b). When we count the number of lattice sites between neighboring misfit dislocations in the IMF we find there are 14 GaAs lattice sites and 13 GaSb lattice sites, in perfect agreement with the literature[15]. All in all, TEM analysis shows that we have grown the world's first GaSb/GaAs(111)A IMF. This IMF efficiently relieves the large compressive strain at the

heteroepitaxial interface to enable subsequent growth of fully relaxed GaSb(111)A films with excellent material quality.

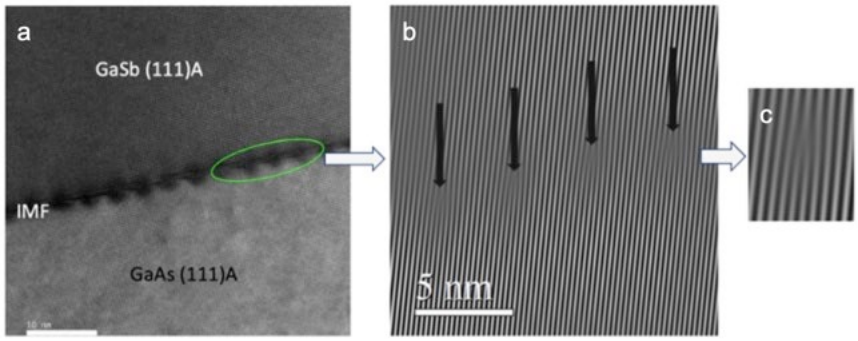

Figure 3.16 a) Zoomed in TEM to show the IMF b) closer view of the IMF c) atomic bond bend to form the IMF

TEM measurements also allowed us to perform EELS analysis on this sample to map elemental composition across the IMF interface. The EELS maps in Figure 3.17 reveal a nice sharp interface with negligible intermixing between Sb and As.

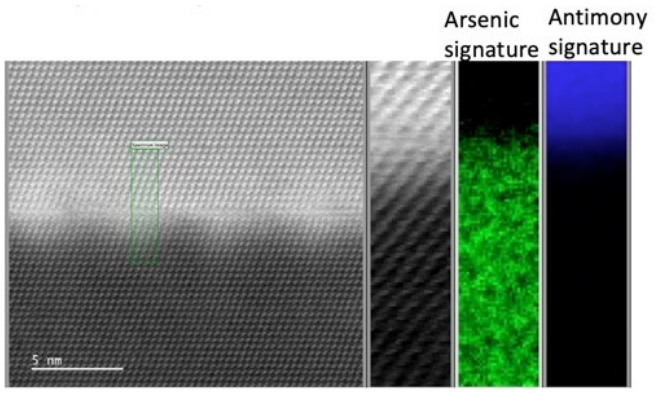

Figure 3.17 EELS of IMF interface region to confirm elemental signatures

While this large defect free region is very promising, this sample was not perfect as we have seen from triangular defects in AFM images. TEM was performed in these defective regions as well to try to understand the nature of these defects and their origin (Figure 3.18).

Figure 3.18a shows that the origin of one of the large triangular defects on the sample surface starts from the region of the IMF. When closer images of this defect are viewed it appears that this is caused by rotated phases of GaSb intersecting and propagating up through the material. Figure 3.18b shows the InAs quantum well as a pale stripe across the image intersected by a vertically propagating twinned region. It appears that this defect of locally affects the InAs growth rate such that the QW here is much thicker than the intended 10nm. This is a critical piece of information because a wider or narrower QW will affect the magnetoresistance results on this structure.

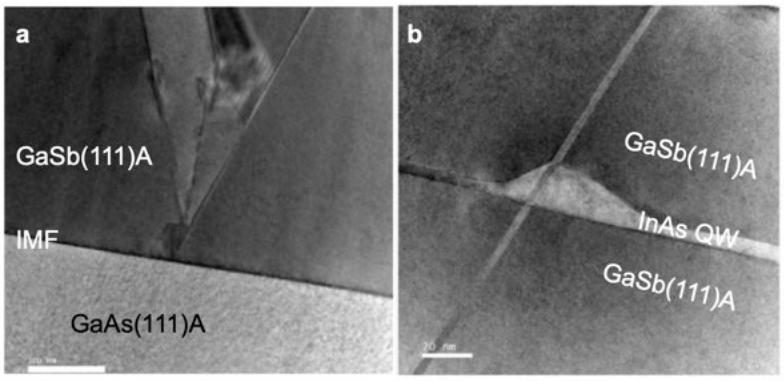

Figure 3.18 TEM of defects in the 4E-6 Torr sample with A) coming from the IMF region and B) coming from the QW region

Longitudinal magnetoresistance measurements were carried out at INL on the 2DEG formed in this InAs/GaSb(111)A QW grown on a GaAs(111)A substrate. Figure 3.19 shows Shubnikov-de Haas oscillations up to 20K. Similar to the results from the InAs/GaSb(001) 2DEG sample in Figure 3.4, the resistance does not fully reach zero in the trough regions, again due to either carrier scattering from defects or parallel conduction. Nevertheless, these oscillations provide evidence that despite the presence of defects, we can clearly resolve subtle effects consistent with quantum transport the

quantum Hall effect in InAs/GaSb(111)A 2DEGs frown on highly mismatched GaAs(111)A substrates. We hope to have the corresponding Hall resistance data soon.

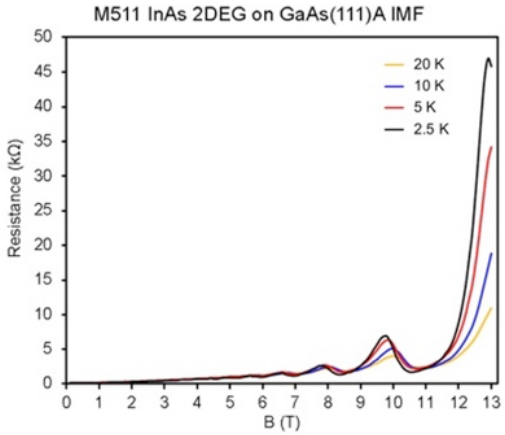

Figure 3.19 Magnetoreistance data on 4E-6 Torr sample showing Shubnikov-de Haas oscillations

Due to the defects observed in these initial GaSb/GaAs(111)A IMF samples, we decided to continue working to optimize the MBE growth conditions in an effort to suppress the formation of these large triangular defects. Given the low growth rates for these samples, we devised a GaSb-based test structure that omitted the InAs QW and doped layers so that more experiments could be done in less time. We evaluated two approaches to reducing these large triangular defects. The first was to insert a GaSb/AlSb superlattice (SL) into the buffer to suppress the propagation of any threading dislocations that form. The second was to reduce the substrate temperature during growth of the first portion of the GaSb buffer to affect the island nucleation in the IMF region and hopefully prevent these defects from forming in the first place. A schematic of these test structures can be seen in Figure 3.20. We grew five test samples based on the structures in Figure 3.20:

1) Control structure of 200nm GaSb
2) SL sample with 5 repeats of 10 nm GaSb/ 10 nm AlSb
3) SL sample with 5 repeats of 5 nm GaSb/ 5 nm AlSb
4) T change sample: 100 nm GaSb at 660°C, 200 nm GaSb at 670°C
5) T change sample: 100 nm GaSb at 650°C, 200 nm GaSb at 670°C

For this work we maintained all the previously established growth conditions. We used a growth rate for the AlSb of 0.13 ML/s to match the GaSb growth rate.

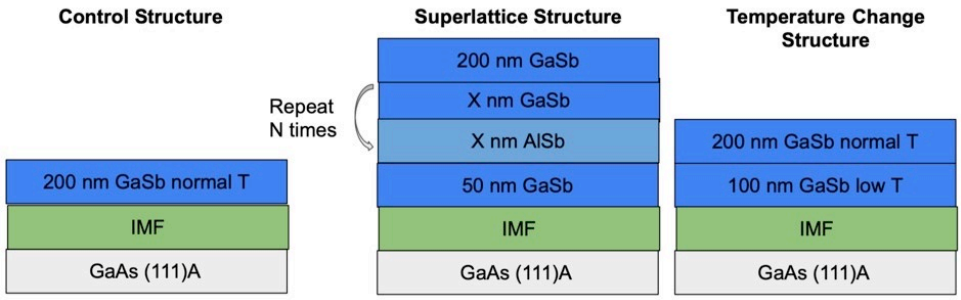

Figure 3.20 Test structures for GaAs (111)A optimization

AFMs from this initial set of experiments is shown in Figure 3.21. These are the large area 50 × 50μm^2 scans performed to assess the overall surface quality. The control sample is reasonably smooth with Rq = 5.19nm but we see crater-like features across the surface (Figure 3.21a). The roughness for the 10nm SL sample is similar at Rq = 5.27nm, but the overall surface appears to be smoother based on the image quality (Figure 3.21b). The 5 nm SL sample was considerably rougher with Rq = 20.9 nm. The surface morphology changes when we introduce the temperature change step, such that the triangular defects seen in previous samples are again present (Figs 3.21 d and e). The roughness value was lower for the sample with a 20°C temperature drop for the initial 100 nm GaSb layer (Fig. 3.21e).

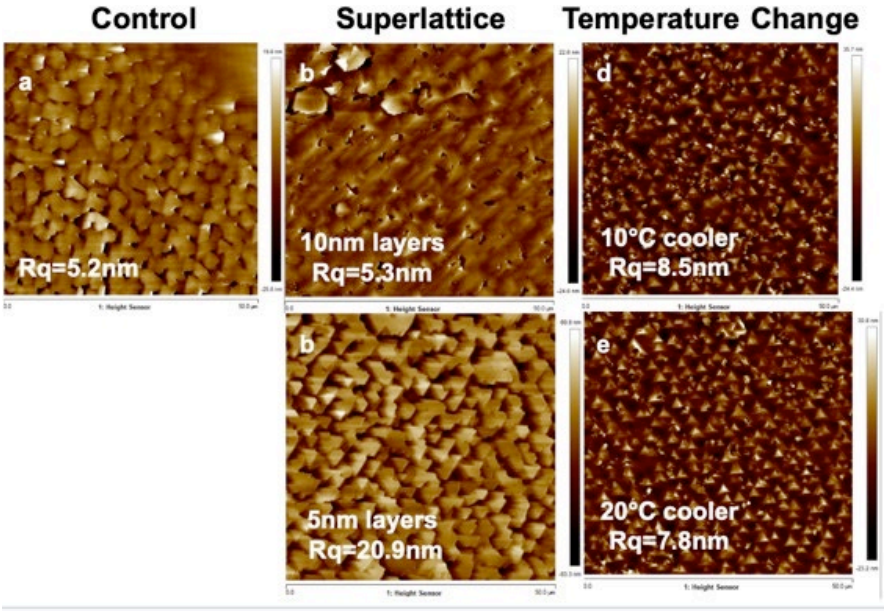

Figure 3.21 50 × 50μm^2 AFM scans for A) control structure, rq=5.19nm, B)10nm SL layers, rq=5.27nm, C) 5nm SL layers, rq=20.9nm, D) 10 degrees cooler, rq=8.48nm, E) 20 degrees cooler, rq=7.81nm

The 2 × 2 μm^2 scans show a clearer picture of the improvements of these samples compared with the control structure (Figure 3.22). At a small scale the roughness on the control structure stays relatively high at Rq = 2.45nm (Figure 3.22a). For the SL that looked best in the 50 × 50 μm^2 scan, the roughness drops to Rq = 0.829 nm, which is a significant improvement, and we can resolve atomic steps despite the presence of defects. For the sample with the 20°C temperature change (Figure 3.22e) Rq drops even further to 0.325nm, with nicely formed atomic steps.

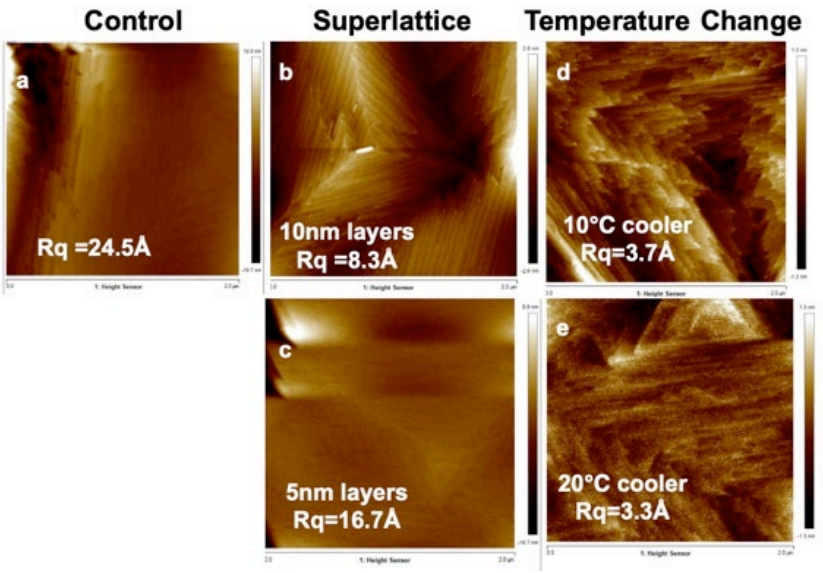

Figure 3.22 2x2μm^2 AFM scans for A) control structure, rq=2.45nm, B)10nm SL layers, rq=0.829 nm, C) 5nm SL layers, rq=1.67 nm, D) 10 degrees cooler, rq=0.366 nm, E) 20 degrees cooler, rq=0.325 nm

Figure 3.23 shows 2θ/ω XRD spectra from these samples. The FWHM values of the GaSb peaks are all similar at 180± 20" suggesting that these changes do not greatly affect crystalline quality of the sample, although the slightly lower values for the SL samples perhaps indicate a modest improvement. XRD from the SL samples also show satellite peaks around the GaSb peak that arise from the repeated GaSb/AlSb layers of the superlattice itself. The spacing of these satellite peaks is a function of the bilayer thickness of each period of the SL and we can use this information to verify that the as-grown sample has the intended layer thicknesses.

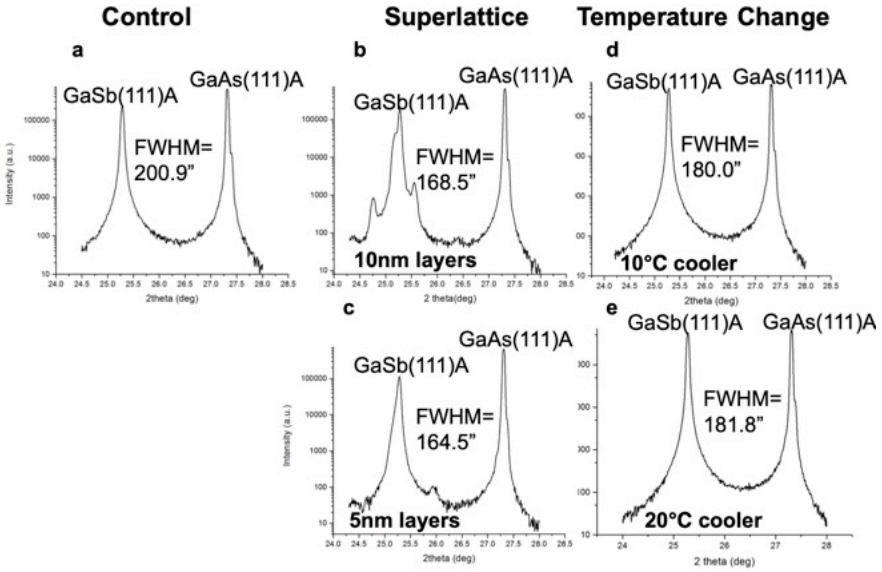

Figure 3.23 XRD 2θ/ω scans for A) control structure, FWHM=200.9", B)10nm SL layers, FWHM=168.5", C) 5nm SL layers, FWHM=164.5", D) 10 degrees cooler, FWHM=180.0", E) 20 degrees cooler, FWHM=181.8"

We also looked at the omega rocking curve scans of the GaSb peak for each sample to assess their FWHM (Figure 3.24). These rocking curve scans show that the 10nm SL sample (FWHM = 350") had a very minor improvement over the control sample (FWHM = 353"), while the 5 nm SL sample was much worse (FWHM = 554"). The temperature change samples showed a much more significant improvement in FWHM. For the sample where the first 100 nm of GaSb was grown 10°C cooler, that improves to FWHM = 245"; growing 20°C cooler reduces it even further to FWHM = 202". These trends are consistent with the changes in surface roughness measured in the $2 \times 2\ \mu m^2$ AFM scans.

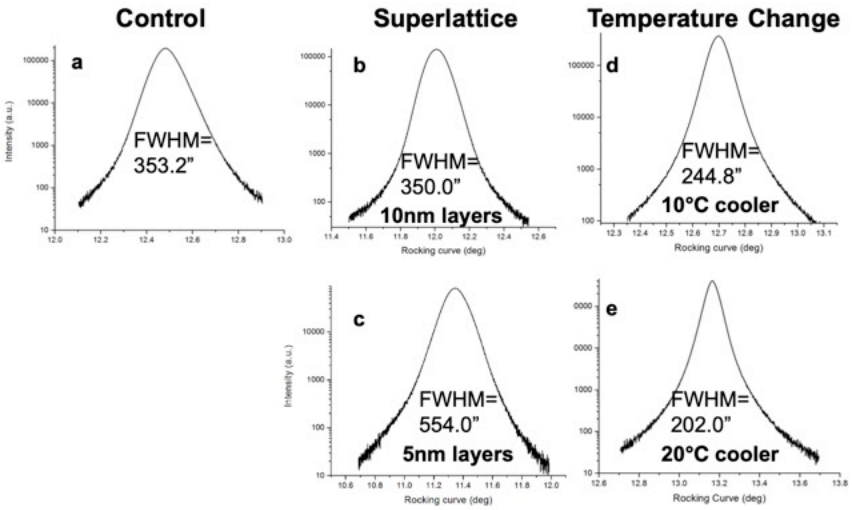

Figure 3.24 XRD Rocking curve scans for A) control structure, FWHM=353.2", B)10nm SL layers, FWHM=350.0", C) 5nm SL layers, FWHM=554.0", D) 10 degrees cooler, FWHM=244.8", E) 20 degrees cooler, FWHM=202.0"

So, from both AFM and XRD it seems that 10 nm SL layers and a 20°C temperature change led to the best GaSb layers. We therefore grew a combined test structure that include both a 10 nm SL and a 20°C temperature change, before finally growing the full doped InAs/GaSb(111)A QW structure on the IMF with optimized conditions. This was done to ensure that when these two elements were combined, they had a net positive effect and did not react negatively in some way. We formed the GaSb/GaAs(111)A IMF 20°C below the optimal temperature for GaSb growth and grew the first 100 nm of the GaSb buffer at this temperature. We then heated the substrate by 20°C to grow another 100nm of GaSb at normal temperature, followed by the 10 nm GaSb/10nm AlSb SL structure. We finished the structure by growing the standard 200nm buffer GaSb layer on top. The 50 × 50 μm^2 and 2 × 2 μm^2 AFM scans from this sample are shown in Figure 3.25.

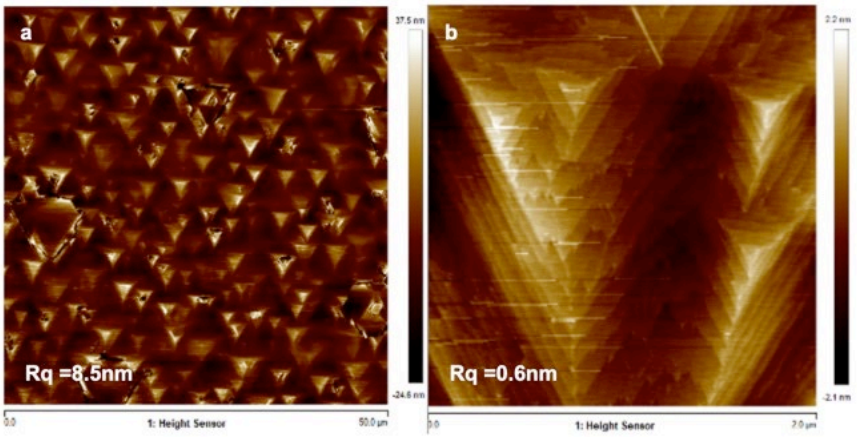

Figure 3.25 A) the 50x50μm^2 AFM scan, rq=8.47nm, B) the 2x2μm scan, rq=0.615nm for the combined SL and temperature change structure.

The roughness value and surface morphology of the large area scan (Figure 3.25a) is consistent with that of the sample containing only the temperature change. For the small area scan (Figure 3.25b), Rq is lower than for the sample containing the SL alone, but higher than the sample containing just the temperature change. Figure 3.26 shows the XRD from this combined sample.

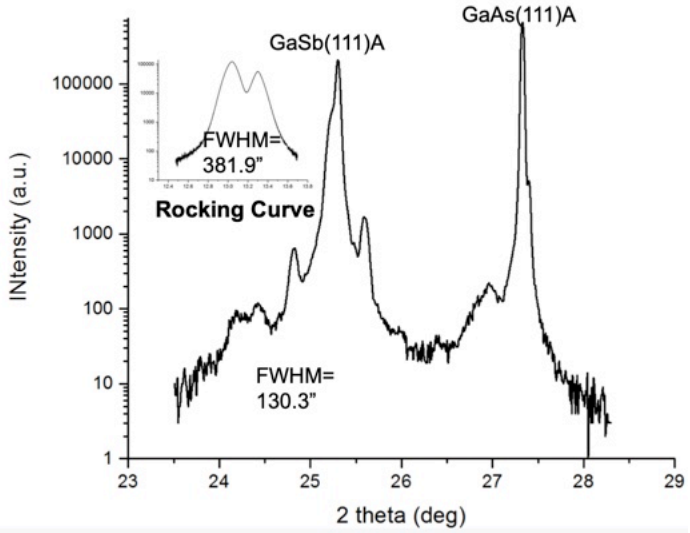

Figure 3.26` XRD scans for combined SL and temperature change test structure with 2θ/ω FWHM=130.3 "and Rocking curve inset FWHM=381.6"

The 2θ/ω scan again shows the satellite peaks around the GaSb from the superlattice and has a FWHM of 130” which is better than any individual previous experiment. The FWHM of the GaSb rocking curve is 382”, which is comparable to the control structure but significantly higher than the sample containing the temperature change alone. We should note that for this sample, the rocking curve shows an unusual double peak which we did not observe on any other sample, and which may be increasing the rocking curve FWHM value. In summary, the XRD and AFM data show that there is no net negative effect from using both techniques to improve our final growth parameters.

Based on the preceding results, we grew two full InAs/GaSb(111)A QW structures on GaSb/GaAs(111)A IMF buffers grown using;

1) the 20°C temperature change only technique
2) the combined SL and 20°C temperature change.

This decision was made due to the drastic decrease in the rocking curve from the temperature change only and the overall benefits seen in the AFM. While some of these elements did not look as beneficial as the control structure alone, we wanted to see the end effects on the final structure and wanted to see if these ended up benefiting the magnetoresistance measurements.

Figure 3.27 shows 50 × 50 μm^2 AFM scans for these two samples containing the full InAs/GaSb QW structure together with the previous best structure grown on a simple GaSb buffer grown under 4E-6 Torr Sb_2 flux. The roughness values for these two samples are Rq = 10.8nm for the combined SL and temperature change sample, while the

temperature change has a Rq = 11.2nm. For comparison, the previous best sample also had Rq = 10.8nm.

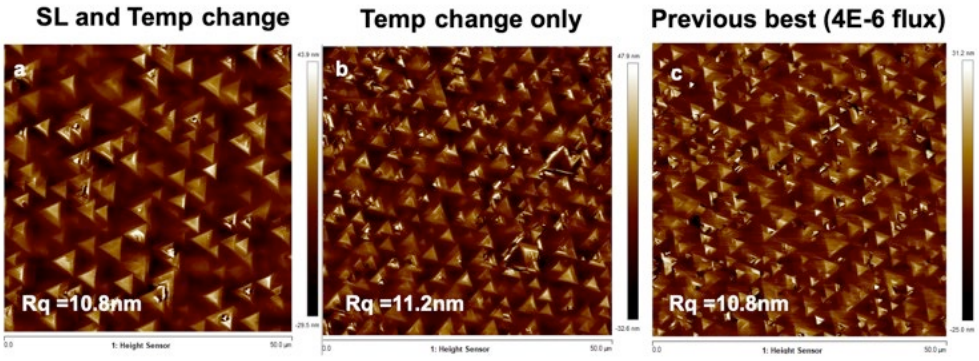

Figure 3.27 50x50μm^{2}AFM scans for A) SL and temp change, rq=10.8nm, B) Temp change only rq=11.2nm, C) previous best sample with 4E-6 flux, rq=10.8nm.

While the surface roughness did not really change, the density of the triangular defects has dropped significantly on the samples grown with the combined SL and temperature change buffer. For the combined SL and temperature change the density of these defects is 0.029 defects/μm^2, for the temperature change only the density is 0.078/μm^2, and for the previous best sample the density is 0.091/μm^2. The density of these defects is significantly lower than the control sample for the SL and temperature change and slightly lower for the temperature change only sample compared to the control, but not such a significant decrease.

Looking at the 2 × 2 μm^2 AFM images we see a similar picture (Figure 3.28). While the Rq value for the previous best sample is an overestimate due to the presence in the image of a crater-like feature, the 1 × 1 μm^2 scan for this sample (not shown) which does not contain this defect still has Rq = 1.35 nm. The new samples with the combined SL/temperature change, and just the temperature change are considerably smoother, with

Rq values of 0.445 nm and 0.327 nm, respectively, indicating that these changes have significantly improved the material quality.

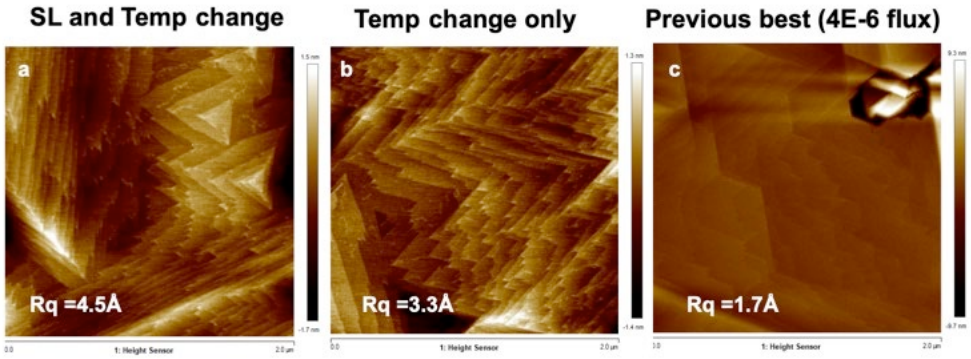

Figure 3.28 2x2μm^2 AFM scans for A) SL and temp change, rq=0.445 nm, B) Temp change only rq=0.327nm, C) previous best sample with 4E-6 flux, rq=1.69nm.

Finally, we measured these samples in XRD with the same Bragg conditions for the 2θ/ω and rocking curve scans previously stated in this section (Figure 3.29). In both cases, the FWHM of the GaSb rocking curve peak is significantly higher than the previous best sample demonstrated. The FWHM of the GaSb 2θ/ω peak stayed consistent across all samples. We suspect the rocking curve FWHM increase could be related to the presence of the SL in the combined sample, as well as to the lower crystal quality of the initial GaSb layer grown at lower temperature to improve the IMF and reduce threading dislocation nucleation and glide.

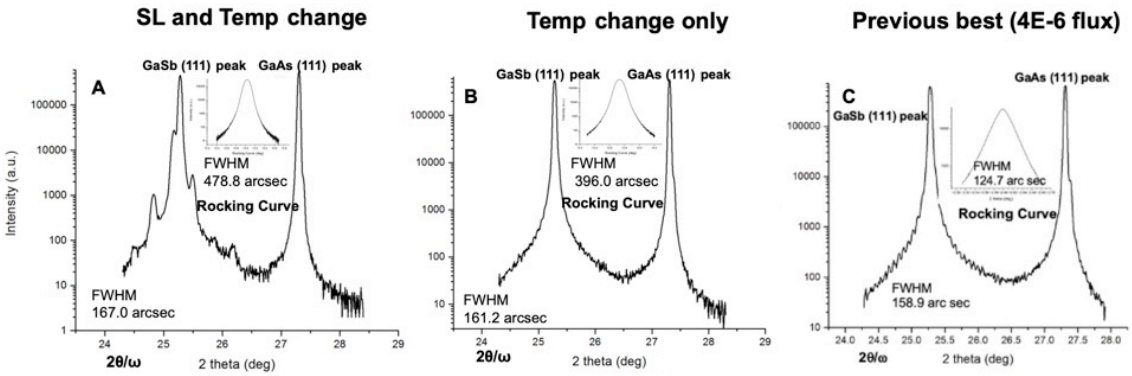

Figure 3.29 XRD scans for A) SL and Temp change, FWHM =478.8", B) Temp change only, FWHM 396.0", C) Previous best sample FWHM=124.7"

Magnetoresistance measurements for these two samples have been performed and are shown below. These measurements show that the changes we made to the GaSb buffer were successful in improving the quality of the material in the InAs/GaSb(111)A QW and hence the quantized electron transport properties of the 2DEG as demonstrated in Fig 3.30. The primary difference that this figure shows is the Shubnikov de Haas oscillations start much lower on these samples, between 4-5T which is on par with the GaSb(001) substrate sample. On the GaAs(111)A samples shown previously the oscillations did not appear until around 9T. Another element shown in these measurements is the overlap of the Hall plateaus with the Shubnikov de Haas oscillations. We can see a nice overlay between the start of a plateau and peak. This further demonstrates that robust quantum Hall effect evident in these samples.

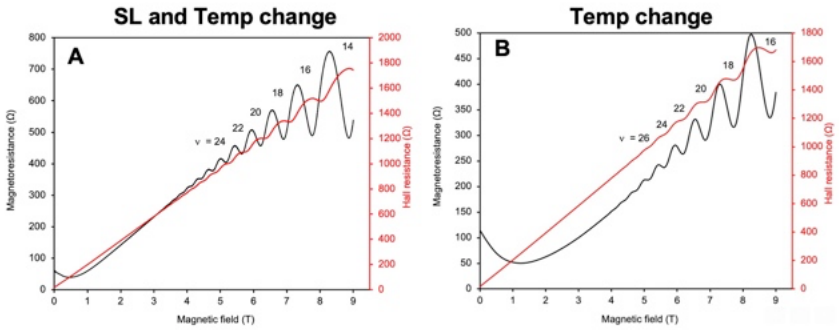

Figure 3.30 Magnetoresistance measurements for A) the SL and temperature change defect filtered sample and B) the temperature change only defect filtered sample.

From the presented thesis research we can conclude that successful growth of InAs/GaSb QWs on GaAs(111)A was performed. We have demonstrated that the structures grown on GaAs(111)A have good FWHM XRD values (124”), better than the best in class values given in the literature for GaAs(001) substrates (240”). These structures also have reasonable AFM roughness values (on the scale of Å for a small area scan). These samples have room for improvement, and our ideas for further improving these samples are detailed in the future work section. Additionally we can see that we have demonstrated the first evidence of the quantum Hall effect on InAs/GaSb QWs grown on GaAs(111)A. The results from the defect filtered samples show both Shubnikov de Haas oscillations as well as Hall plateaus indicating robust measurements. These facts show that we have successfully accomplished the research goals that we set out to achieve with this thesis work.

FUTURE WORK

At this stage of the project a majority of the future work of interest reliant on the full set of results from the 2DEG magnetoresistance measurements that we are waiting on. If we see that the electron transport in InAs/GaSb QWs grown on either GaSb(111)A or GaAs (111)A looks particularly interesting, for example in terms of high mobility, or high temperature quantum effects, I would like to explore the MBE conditions needed to grow those samples to see if further improvements are possible.

In addition, I would like to try using offcut GaAs(111)A substrates for these growths, and compare the corresponding magneto resistance results and TEM images from those samples with the existing work that has been performed. It is possible that these offcut substrates could limit the large triangular defects that we observed for many of these samples in AFM[45]. If this were possible, I would like to evaluate the change in surface morphology due to substrate offcut, as well as any change in the magnetoresistance measurements. Any differences would be very informative regarding the effect these triangular defects have, and suggest ways to improve the quantum transport properties of these 2DEGs even further.

I would also like to try performing photoluminescence (PL) measurements on these samples as it can provide information about the quantum behavior of the InAs/GaSb QWs. Electrons excited into the InAs 2DEG by a laser will recombine with holes in the GaSb barrier. The wavelength of the photons emitted by this recombination process will give us more information about the band structure of these 2DEG samples.

Since crystal quality is often linked to optical performance, comparing the intensity of the PL signal between samples will allow us to talk about the impact of the surface orientation and the presence of an IMF on the quality of the InAs 2DEG. I would be interested to evaluate the PL results against the magnetoresistance measurements to understand if this could be used to gauge the same type of information as the magnetoresistance measurements. If it could, PL could be a quicker way to evaluate good samples from bad before taking the time to do the full quantum Hall effect measurements which take significantly longer.

If all the characterization measurements indicate that the 2DEG material is of sufficient quality, I would like to proceed by making and testing devices with the materials that have been grown here. This would provide the ultimate test of sufficient material quality and would help realize the actual applications we introduced at the beginning of this thesis. For example, I would like to explore electron transport in both the Γ and L valleys to see if we can overcome the density of states bottleneck for future high speed III-V transistor applications.

REFERENCES

1. Mehrotra, S. R. *et al.* Simulation study of thin-body ballistic n-MOSFETs involving transport in mixed Γ-L valleys. *IEEE Electron Device Letters* **34**, 1196–1198 (2013).

2. Yerino, C. D., Liang, B., Huffaker, D. L., Simmonds, P. J. & Lee, M. L. Review Article: Molecular beam epitaxy of lattice-matched InAlAs and InGaAs layers on InP (111)A, (111)B, and (110). *Journal of Vacuum Science & Technology B, Nanotechnology and Microelectronics: Materials, Processing, Measurement, and Phenomena* **35**, 010801 (2016).

3. Eyink, K. G. *et al.* Electrical and structural characterization of a single GaSb⁄InAs⁄GaSb quantum well grown on GaAs using interface misfit dislocations. *J Appl Phys* **104**, 074901 (2008).

4. Reyner, C. J. *et al.* Characterization of GaSb/GaAs interfacial misfit arrays using x-ray diffraction. *Appl Phys Lett* **99**, 231906 (2011).

5. Band structure and carrier concentration of Gallium Antimonide (GaSb). https://www.ioffe.ru/SVA/NSM/Semicond/GaSb/bandstr.html.

6. Abedin, M. A SELF-ADJUSTING LIN-LOG ACTIVE PIXEL FOR WIDE DYNAMIC RANGE CMOS IMAGE SENSOR Department of Electrical and Electronic Engineering Chittagong University of Engineering and. (2016) doi:10.13140/RG.2.1.3871.8965.

7. Roul, B., Kumar, M., Rajpalke, M. K., Bhat, T. N. & Krupanidhi, S. B. Binary group III-nitride based heterostructures: Band offsets and transport properties. *J Phys D Appl Phys* **48**, (2015).

8. Downs, C. & Vandervelde, T. E. Progress in infrared photodetectors since 2000. *Sensors (Switzerland)* **13**, 5054–5098 (2013).

9. 22.11: Metal Oxide Semiconductor Field Effect Transistor (MOSFET) - Engineering LibreTexts. https://eng.libretexts.org/Bookshelves/Materials_Science/TLP_Library_II/22%3A_Introduction_to_Semiconductors/22.a11%3A_Metal_Oxide_Semiconductor_Field_Effect_Transistor_%28MOSFET%29.

10. Stephens, G. Two Dimensional Electron Gas, Quantum Wells & Semiconductor Superlattices.

11. Digital Integrated Circuits Analysis and Design MOS Transistor.

12. Simmonds, P. J. *et al.* Quantum transport in In0.75Ga0.25As quantum wires. *Appl Phys Lett* **92**, 152108 (2008).

13. Blinder, S. M. Classical and Quantum Hall Effects - Wolfram Demonstrations Project. https://demonstrations.wolfram.com/ClassicalAndQuantumHallEffects/ (2020).

14. Simmonds, P. Molecular Beam Epitaxy of InGaAs and InAlAs for Low-Dimensional Electrical Transport. (University of Cambridge, 2007).

15. Jallipalli, A. *et al.* Atomistic modeling of strain distribution in self-assembled interfacial misfit dislocation (IMF) arrays in highly mismatched III–V semiconductor materials. *J Cryst Growth* **303**, 449–455 (2007).

16. (1) (PDF) Nitride-based semiconductor nanostructures for applications in optical communications at 1.5 um. https://www.researchgate.net/publication/281452125_Nitride-based_semiconductor_nanostructures_for_applications_in_optical_communications_at_15_um.

17. MBE - Molecular Beam Epitaxy. https://warwick.ac.uk/fac/sci/physics/current/postgraduate/regs/mpagswarwick/ex5/growth/pvd/.

18. Agarwal, D. H., Bhatt, P. M., Pathan, A. M., Patel, H. & Joshi, U. S. Development of portable experimental set-up for AFM to work at cryogenic temperature. *AIP Conf Proc* **1447**, 531–532 (2012).

19. The Transmission Electron Microscope | CCBER. https://www.ccber.ucsb.edu/ucsb-natural-history-collections-botanical-plant-anatomy/transmission-electron-microscope.

20. Hachtel, J. A., Lupini, A. R. & Idrobo, J. C. Exploring the capabilities of monochromated electron energy loss spectroscopy in the infrared regime. *Sci Rep* **8**, (2018).

21. Naresh-Kumar, G. *et al.* Electron channelling contrast imaging for III-nitride thin film structures. *Mater Sci Semicond Process* **47**, 44–50 (2016).

22. Klitzing, K. v., Dorda, G. & Pepper, M. New Method for High-Accuracy Determination of the Fine-Structure Constant Based on Quantized Hall Resistance. *Phys Rev Lett* **45**, 494 (1980).

23. Dem'yanenko, M. A. *et al.* AlGaAs/GaAs Quantum Well Infrared Photodetectors. *Two-dimensional Materials for Photodetector* (2017) doi:10.5772/INTECHOPEN.71266.

24. Mu, X., Sullivan, G. & Du, R.-R. Effective g-factors of Carriers in Inverted InAs/GaSb Bilayers.

25. Andrews, A. M. *et al.* THz Quantum Cascade Lasers. *Molecular Beam Epitaxy* 597–624 (2018) doi:10.1016/B978-0-12-812136-8.00028-1.

26. Thomas, C. *et al.* High mobility InAs 2DEGs on GaSb substrates: a platform for mesoscopic quantum transport.

27. Kroemer, H. The 6:1 A family (InAs, GaSb, AlSb) and its heterostructures: a selective review. *Physica E* **20**, 196–203 (2004).

28. Schmid, S. *et al.* Exploring the phase diagram of InAs/GaSb/InAs trilayer quantum wells. *Phys Rev B* **105**, 155304 (2022).

29. Zakharova, A., Semenikhin, I. & Chao, K. A. Spin-related phenomena in InAs/GaSb quantum wells. *JETP Lett* **94**, 660–664 (2011).

30. Wickramasinghe, K. S. *et al.* Transport properties of near surface InAs two-dimensional heterostructures. *Appl Phys Lett* **113**, 262104 (2018).

31. Kim, R., Rakshit, T., Kotlyar, R., Hasan, S. & Weber, C. E. Effects of surface orientation on the performance of idealized IIIV thin-body ballistic n-MOSFETs. *IEEE Electron Device Letters* **32**, 746–748 (2011).

32. Mokkapati, S. & Jagadish, C. III-V compound SC for optoelectronic devices. *Materials Today* **12**, 22–32 (2009).

33. Yuan, L.-D., Deng, H.-X., Li, S.-S., Luo, J.-W. & Wei, S.-H. Unified theory of the direct or indirect bandgap nature of conventional semiconductors.

34. Sands, T. *et al.* Stable and epitaxial metal/III-V semiconductor heterostructures. *Materials Science Reports* **5**, 99–170 (1990).

35. 3.5: The Energy of a Particle in a Box is Quantized - Chemistry LibreTexts. https://chem.libretexts.org/Bookshelves/Physical_and_Theoretical_Chemistry_Textbook_Maps/Physical_Chemistry_(LibreTexts)/03%3A_The_Schrodinger_Equation_and_a_Particle_in_a_Box/3.05%3A_The_Energy_of_a_Particle_in_a_Box_is_Quantized.

36. Hall effect | Definition & Facts | Britannica. https://www.britannica.com/science/Hall-effect.

37. Tsui, D. C., Stormer, H. L. & Gossard, A. C. Two-dimensional magnetotransport in the extreme quantum limit. *Phys Rev Lett* **48**, 1559–1562 (1982).

38. Carlos De Andrade Getelina, J. Quantum Hall Effects. (2018).

39. Jasik, A. *et al.* Comprehensive investigation of the interfacial misfit array formation in GaSb/GaAs material system. *Appl Phys A Mater Sci Process* **124**, 1–12 (2018).

40. Ohtake, A., Mano, T., Mitsuishi, K. & Sakuma, Y. Strain Relaxation in GaSb/GaAs(111)A Heteroepitaxy Using Thin InAs Interlayers. *ACS Omega* **3**, 15592–15597 (2018).

41. Deitz, J. I., Grassman, T. J., Mccomb, D. W., Ghazisaeidi, M. & Niezgoda, S. Bridging the Gap: Probing Structure-Property Relationships in Functional Materials through Advanced Electron Microscopy Based Characterization.

42. Electron channelling contrast imaging (ECCI) – Semiconductor Spectroscopy and Devices. https://ssd.phys.strath.ac.uk/techniques/scanning-electron-microscopy/electron-channelling-contrast-imaging-ecci/.

43. Huang, S. H. *et al.* Strain relief by periodic misfit arrays for low defect density GaSb on GaAs. *Appl Phys Lett* **88**, 131911 (2006).

44. Vallejo, K. *et al.* Tensile-strained InGaAs quantum dots with interband emission in the mid-infrared. *In preperation*.

45. Sadeghi, I., Tam, M. C. & Wasilewski, Z. R. On the optimum off-cut angle for the growth on InP(111)B substrates by molecular beam epitaxy. *Journal of Vacuum Science & Technology B, Nanotechnology and Microelectronics: Materials, Processing, Measurement, and Phenomena* **37**, 031210 (2019).

46. Seth R. Bank – What is MBE? – UT-Austin. https://lase.mer.utexas.edu/mbe.php.